Institute of Physics

Faculty of Mathematics, Physics and Chemistry

University of Silesia

Julita Piecha

Ph.D. Thesis

Segregation of ions in surface layer of the $LiNbO_3$ single crystal induced by proton exchange reaction and by thermal treatment

Key words:

congruent lithium niobate,
proton exchange,
surface layer,
SIMS, XPS

Doctoral Supervisor:

Dr hab. Andrzej Molak

Katowice, 2016

Abstract

Lithium niobate is a ferroelectric crystal obtained by the Czochralski's method. It has a rhombohedral structure with space group *R3c*. $LiNbO_3$ exhibits high Curie temperature (T_C≈1120 °C) and melting point (T_m≈1230 °C). The aim of my research was to determine the influence of the proton exchange reaction and the reduction conditions on the lithium segregation in the surface layer of the congruent $LiNbO_3$. The high mobility of the lithium ions in the surface layer and their migration from the interior part of the crystal to the surface was presumed in the ion exchange of Li^+/H^+. Proton exchange reaction was carried out in the specially-assembled patented apparatus. The protonization reaction was carried out in an environment of the concentrated HNO_3(V). The depth profiles were obtained from the SIMS measurement to show the ions substitution. The concentrations of the lithium and the niobium ions contained in the reaction solution were checked by the ICP-OES technique. The XRD test showed that for pure $LiNbO_3$ crystal structure was maintained and for protonized sample, $H_xLi_{1-x}NbO_3$, the identified structure was monoclinic. The electric features pointed that activation energy decreased for the protonized $LiNbO_3$. Brillouin spectroscopy enabled to determine Curie's temperature T_C=1120 °C and showed the influence of the protonized surface layer on the volumetric response of the crystal. The pure $LiNbO_3$ was analyzed by the XPS (at RT and in the temperature range from 300 to 900 °C) in order to determine the chemical composition of the crystal. The significant deficiency of the lithium ions was detected at the RT in the epi-polished surface layer. Concentration was given by the [Li]/[Nb]=0.04 ratio and in the cleaved surface of the crystal [Li]/[Nb]=0.67. Differences between received [Li]/[Nb] ratio, in terms of literature data, may indicate the existence of easy diffusion paths, in addition to the point defects. Low stability of the lithium ions, and non-homogenous composition in the surface layer of the samples treated with the high temperature in a reduced atmosphere, were confirmed by the: XPS, TGA, effusion, SIMS, ICP-OES, and XRD techniques. The XPS test exhibited lack of the Li 1s state in the temperature range of the 300–500 °C, Li 1s state emergent at T=700 °C. The TGA measurement showed an influence of the reduction conditions in the mass losses, and a change in the transparency of the crystal. Effusion test conducted at the 800 and 900 °C allowed identification of the gaseous species released from the sample, *e.g.*, Li_2O and O_2. The SIMS maps exhibited non-homogenous distribution of the elements in the surface of the reduced crystals. The depth profiles showed changes in the [Li]/[Nb] ratio for temperature of the 750, 850, and 950 °C. The outward diffusion of the Li ions was proven. The conditions of formatting $H_xLi_{1-x}NbO_3$ were determined.

Streszczenie

Niobian litu to ferroelektryczny kryształ otrzymywany metodą Czochralskiego, wykazuje on strukturę romboedryczną z grupą przestrzenną *R3c*. Charakteryzuje się wysokimi wartościami temperatury Curie (T_C≈1120 °C) oraz temperatury topnienia (T_m≈1230 °C). Celem moich badań było określenie wpływu reakcji protonizacji oraz redukcji na segregację jonów litu w warstwie powierzchniowej kongruentnego $LiNbO_3$. Wysoką mobilność jonów litu w warstwie powierzchniowej oraz ich migrację z wnętrza kryształu ku jego powierzchni wykorzystano w procesie wymiany jonowej Li^+/H^+. Reakcję wymiany protonowej prowadzono w specjalnie skompletowanej aparaturze chemicznej objętej patentem. Wpływ reakcji protonizacji, przeprowadzonej w środowisku stężonego HNO_3(V) przedstawiono w formie profili głębokościowych SIMS. Na podstawie analizy danych ICP-OES określono stężenie jonów litu i niobu znajdujących się w roztworze kwasu, w którym prowadzono reakcję. Badaniami XRD potwierdzono strukturę czystego niobianu litu, natomiast próbka protonizowana, $H_xLi_{1-x}NbO_3$, wykazała strukturę jednoskośną. Badania elektryczne wykazały wpływ procesu protonizacji na obniżenie wartości energii aktywacji modyfikowanych próbek. Wykorzystując technikę Brillouin'owskiego rozpraszania światła wyznaczono temperaturę Curie T_C=1120 °C, oraz wykazano wpływ protonizowanej warstwy powierzchniowej na badania objętościowe. Próbkę czystego $LiNbO_3$ poddano analizie XPS (w RT oraz w zakresie temperatur od 300 do 900 °C) celem określenia jej składu chemicznego. Zaobserwowano znaczny niedobór jonów litu zarówno w warstwie powierzchniowej [Li]/[Nb]=0.04 oraz na krawędzi przełomu kryształu [Li]/[Nb]=0.67. Różnice otrzymanych wartości stosunku [Li]/[Nb], względem wartości literaturowych, mogą świadczyć o istnieniu bardziej złożonych form zdefektowania, np. ścieżek łatwej dyfuzji, a nie tylko defektów punktowych. Niewielka stabilność jonów litu i brak jednorodności w warstwie powierzchniowej próbek poddanych obróbce termicznej w redukującej atmosferze potwierdzono przy użyciu technik: XPS, TGA, efuzji, SIMS, ICP-OES oraz XRD. Analiza XPS ukazała brak stanu Li 1s w warstwie powierzchniowej w przedziale 300–500 °C, uwidocznił się on w T=700 °C. Badania TGA ukazały ubytek masy oraz zmianę transparentności analizowanego materiału. Efuzja prowadzona w temperaturach 800 i 900 °C umożliwiła identyfikację uwolnionych z próbki gazowych produktów, np. Li_2O i O_2. Mapy SIMS przedstawiły niehomogeniczny rozkład litu i niobu w warstwie powierzchniowej. Uzyskane wyniki pozwoliły na wyznaczenie wartości oraz zmian w stosunku [Li]/[Nb] na profilach głębokościowych dla 750, 850 i 950 °C. Dyfuzja jonów Li została potwierdzona. Warunki formowania $H_xLi_{1-x}NbO_3$ zostały określone.

Acknowledgments

I express my deepest gratitude to dr hab. Andrzej Molak for shearing a time and knowledge in multiple conversations which have been an inspiring lessons throughout my journey to PhD degree.

I am thankful to prof. dr hab. Krzysztof Szot for the knowledge and wisdom that have imparted upon me, great help and support for motivating me to pursue my goals with hard work and dedication.

Also I am thankful to prof. dr hab. Krystian Roleder for encouragement when I need the most and for constantly inspiring me to challenge myself.

I thank all co-workers from Department of Ferroelectrics Physics and other departments of our University for sharing their experiences.

I thank my family for patient and continually support, primary my sister for all her time and everlasting believing in me.

Table of contents

1 Introduction

1.1 Motivation

The protonization process and ion segregation in the surface of the lithium niobate is still an open subject for research. Protonization leads to formation of $H_xLi_{1-x}NbO_3$ compound. As the final product, unique solid state acid $HNbO_3$ can be obtained. Therefore, it was an inspiring subject of analysis.

The lithium niobate crystals are applied both in their pure and with modified physical and chemical treatment forms. One can distinguish crystal samples with an epi-polish surface used for their electro-optic applications, which can be also used as a substrate in deposition of thin films, and protonized crystals with better surface acoustic features. It is difficult to make a proper preparation of the sample without making significant changes in the stoichiometry of the surface layer. For instance, high-quality electro-optical and nonlinear optical devices based on the $LiNbO_3$ require an extremely accurate constant [Li]/[Nb] ratio, *i.e.*, congruent composition, to ensure birefringence homogeneity in case of the lithium ions migration. It is worth to notice that chemical composition and structure of the surface layer is an important factor which influences the actual properties of the lithium niobate.

My aim was to check how much and to what extent the proper preparation can change the surface of the lithium niobate crystals. It was necessary to verify whether or not the actual surface layer chemical composition differs from the initial composition of the congruent crystal. I presumed that modification of the lithium niobate crystals occurred on their surface layer. I tried to explain the deficiency of the lithium ions in the crystal's surface layer in case of existence of the paths dislocations. High mobility of the lithium ions has a significant impact on congruency of lithium niobate.

In my research, I studied an influence of the proton exchange reaction and thermal treatment on the surface of the $LiNbO_3$. For that reason, I carried out a physico-chemical analysis of the lithium niobate surface layer using several methods. Proton exchange reaction was carried out in a specially-assembled chemical patented apparatus. Protonized crystal samples and solutions of the conducted reaction should be analysed with the use of the SIMS and ICP-OES techniques, respectively. The XRD test should verify if the pure $LiNbO_3$ crystal structure is maintained, or not, for protonized samples of the $H_xLi_{1-x}NbO_3$. Brillouin spectroscopy should determine the Curie's temperature and the influence of the

protonization on the crystal response. The atomic concentration of the $LiNbO_3$ can be verified in the XPS *in-situ* measurement. The TGA test should show an influence of reduction conditions on the mass changes. Effusion test should allow to identify gaseous species released from the sample. The SIMS analysis should describe ion distribution in the surface layer of the crystal.

1.2 Ferroelectric materials

The crystal is ferroelectric when has two or more orientation states in the absence of an electric field and can be shifted from one state to another by an electric field. The ferroelectric material shows a spontaneous polarization P_s which decreases with increasing temperature T to disappear continuously, or more often discontinuously, at a Curie's point T_C [1]. The polarization can be reversed by applying a sufficiently large electric field. In a strong alternating field, it therefore shows hysteresis (see Figure 1). The ferroelectric materials changes to non-polar above the transition temperature (Curie's point) [2]. Representatives of the ferroelectric materials are, *e.g.*, Rochelle salt, barium titanate, lithium niobate.

Classification of the ferroelectric materials:

- Displacive ferroelectrics are materials where the ferroelectric transition could be described as the result of an instability of the anharmonic crystal lattice against a soft polar lattice vibration. The discrete symmetry group is broken at T_C.
- Order – disorder type ferroelectric characterized by broken discrete symmetry grupe due to ordering an ions in a strong anharmonic rigid multisite lattice potential
- Ferroelectric liquid crystals, where continuous symmetry group is broken at the T_C and the doubly degenerate relaxational soft mode in the high – temperature phase splits below T_C into an "amplitudon" – type soft mode and symmetry – restoring Goldstone mode.
- Relaxors, where there is no macroscopic symmetry breaking and where in a view of the "site" and "charge" disorder, there is an extremely broad distribution of the correlation times. The longest correlation times diverges at the freezing transition, whereas other correlation times are still finite. The

glassy order and an Edwards – Anderson order parameters are preferred over than classical ferroelectric long-range order. Instead of a spontaneous polarization, we deal with a polarization distribution function with zero mean value [3].

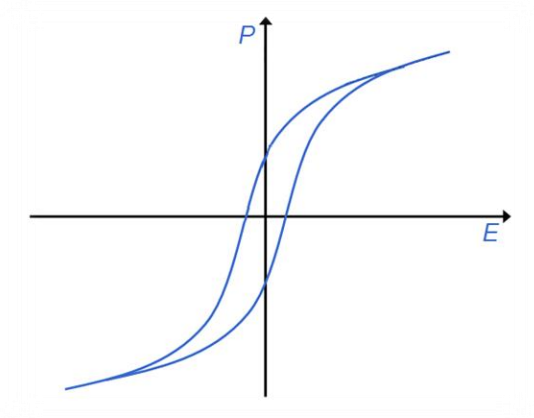

FIG. 1 Ferroelectric hysteresis loop.

One of the basic quantities characterizing the material is dielectric permittivity.

$$\varepsilon = \frac{\partial D}{\partial E}. \tag{1a}$$

This quantity describes a response of the dielectric material on the applied electric field. It is described by:

$$\varepsilon^* = \varepsilon_r^* \varepsilon_0, \tag{1b}$$

where ε_r is the relative permittivity of the material. The ε_0 is the vacuum permittivity and it is equal to ε_0=8.85× 10^{-12} F/m.

For isotropic materials, we can treat it as the scalar quantity, but in general, it is second order symmetric tensor. For materials with relaxation polarization, the permittivity is the size complex, which has the polar and loss contribution:

$$\varepsilon_r^* = \varepsilon_r' - i\varepsilon_r'', \tag{1c}$$

where ε' (the real part of permittivity) determines stability to store the energy. The ε'' (the imaginary part of permittivity), which corresponds to the resistance and describes the energy losses in the system [4].

For non-polar dielectric the permittivity decreases with increasing temperature due to the decreased number of the atoms per unit volume, whereas for most of the dielectric with the ionic structure the permittivity increases with increasing temperature. Most of these crystals show that the value of the relative permittivity is lower than a few dozens. In ferroelectric crystals, the dielectric permittivity reaches a much higher value.

The tangent of the angle between ε' and ε'' is called dielectric loss angle:

$$tg\delta = \frac{\varepsilon''}{\varepsilon'}. \tag{2}$$

This quality describes the energy losses occurring as a result of the occurrence of the internal resistance which shows the system flowing current. The angle can be described as the phase shift between the changes in the electric field and the electric displacement field.

$$E = E_0 \cos(\omega t) \tag{3}$$

$$D = D_0 \cos(\omega t - \delta). \tag{4}$$

The tangent of the loss varies with the frequency of the electric field and therefore a capacitor filled, with a dielectric, can be described by the equivalent circuit, wherein the power dissipation would be equal to the power dissipated on the capacitor with resistor (circuit RC). The losses showed the marked dispersion when crystals were containing defects.

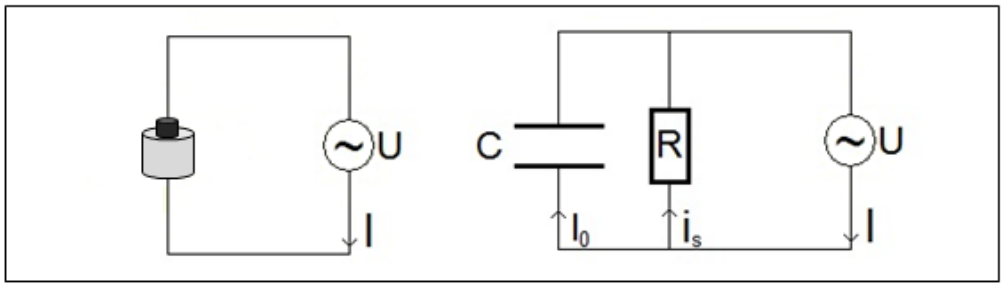

FIG. 2 The measuring circuit with teflon tube filled with the $LiNbO_3$ and equivalent circuit.

The relative dielectric permittivity, ε_r, is determined by the calculation of the ratio of the capacity of the capacitor filled with dielectric C to capacity measured in the vacuum C_0. This quantity is unitless and real.

$$\varepsilon_r = \frac{C}{C_o}. \tag{5a}$$

The imaginary part of dielectric permittivity ε_r'', is related to electric conductivity:

$$\varepsilon_r'' = \frac{\sigma}{\omega \varepsilon_0}. \tag{5b}$$

1.3 Surface imperfections

Defects on oxide surfaces are often produced during cutting a crystal, cleaning it by ionic bombardment, and annealing at high temperature. It is very difficult to prepare a stoichiometric and structurally perfect surface. The surface treatments favor the creation of the geometrical defects, such as steps, or stoichiometry defects such as oxygen or cation vacancies. When a crystal is cut along chosen orientation, the atoms located in the few outer layers experience non-zero forces, which, are induced by the breaking of oxygen-cation bonds. Generally, they do not remain at the positions fixed by the three-dimensional lattice. Point and extended defects may result, as well as lattice distortions. Many experiments in the past have been performed, unwittingly, on imperfect surfaces and some of their results, for example those concerning the presence of intrinsic surface states, are questionable. More recent studies have been performed with a more rigorous control of the surface stoichiometry and are thus free of these limitations. The interest in the surface defects on the oxides also relies on considerations of reactivity, since steps or vacancies (see Figure 3) are known to be active centers for chemical reactions [5].

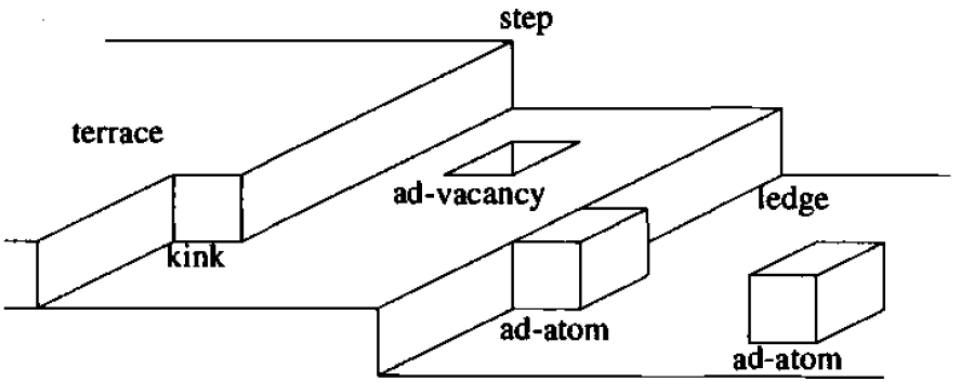

FIG. 3 Defects on the surface [5].

However, the detailed characterization of the surface layer chemical composition is scarce. Therefore, the analysis of chemical changes in the surface layer of double oxide materials, induced by the thermal conditions and/or applied electrical fields, shows the present-day direction of research [6, 7, 8, 9, 10, 11, 12, 13]. After a purposeful thermal treatment, the surfaces of the crystals exhibit wide variations in chemical composition. These changes can be explained on the basis of the defect formation, *e.g.*, point defects, clusters and extended defects generation [14, 15, 16, 17, 18, 19, 20].

1.4 $LiNbO_3$ crystal features

Lithium niobate is a ferroelectric crystal synthesized for the first time in 1949, it is an excellent material with wide range usage due to physical field of nonlinear, electro-optic, piezoelectric, acoustical, and photorefractive properties, high electro-optic coefficient, transparency range. There is a lot of applications of the lithium niobate in the fields such as: linear and nonlinear optical devices, acousto-optic modulators, second-harmonic generation, integrated optics applications, bulk and waveguide optoelectronic devices due to low acoustic losses. Lithium niobate occupies an important place in the field of laser materials reported for the first time pulsed stimulated emission by using the Nd-doped congruent lithium niobate crystals in 1969 [21, 22].

The $LiNbO_3$ is colourless, chemically stable, and insoluble in liquid solvents like water or organic solution material with high melting point. The $LiNbO_3$ crystal is uniaxial at all temperature range, and it exhibits only one structural phase transition. At the room temperature, the crystal is a ferroelectric material with rhombohedral (trigonal) structure, which corresponds to the space group *R3c*, with point group *3m* (see Figure 4). The Li^+ ions are shifted with respect to the oxygen plane by 44 pm, and the Nb^{5+} ions are shifted with respect to the centre of the octahedron by 26-27 pm. Above the Currie's temperature T_C=1140 °C, the crystal transforms to the paraelectric phase (see Figure 5) and changes symmetry to the centrosymmetric space group *R3m*. In nonpolar phase, the Li^+ ions are localized within the oxygen planes, and the Nb^{5+} ions are in the center of the oxygen octahedra. The lithium octahedron is larger than the niobium. Responsible for this situation is a distance between lithium ion and the two closest oxygen ions, which are equal to 206.8 and 211.2 pm, and for niobium ions the distance is equal to 188.9 and 211.2 pm [23]. The large size of the lithium octahedron may qualitatively explain a predominant incorporation

of the impurity ions into lithium sites [14]. Lithium niobate exhibits second-order phase transition [1].

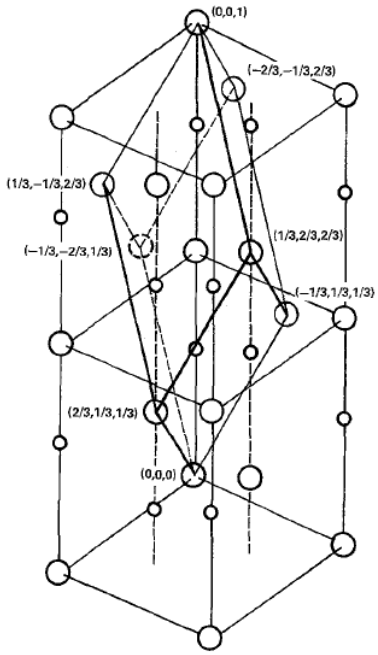

FIG. 4 Conventional rhombohedral unit cell of lithium niobate shows with respect to the hexagonal unit cell [24].

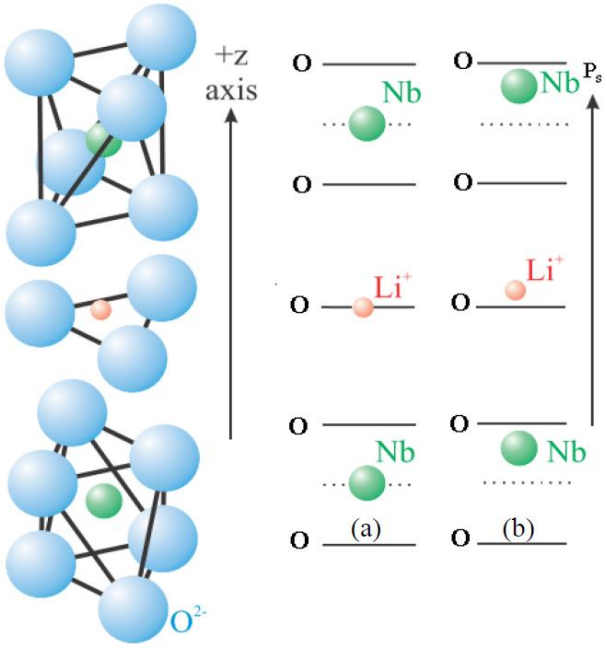

FIG. 5 Schematic structure of lithium niobate (a) paraelectric phase (b) ferroelectric phase [24].

The threefold axis is placed along *z* direction, the *y*-axis lies in the mirror plane and the *x*-axis is orthogonal to both of them. The *z* and *y*-axes are polar (piezoelectric), the *z*-axis is also pyroelectric. In accordance to this label, the *x*-axis is non-polar.

The quality of the surface layer ought to be verified when the crystal material is concerned for applications. For instance, the waveguides, frequency modulators performed on the lithium niobate surface are extensively studied.

1.5 Recent studies on protonized $LiNbO_3$

The proton exchange reaction is commonly used to aim the induce velocity decrease for the surface acoustic wave (SAW) propagation [25], to modify piezoelectric and electro-optic properties in fabrication of the waveguides [26, 27, 28, 29, 30, 31, 32], and for accumulation of the charge carriers [33]. The rate and the completeness of the performed substitution was checked by the XRD tests, which showed coexistence of the rhombohedral and cubic phases, dependably on the thermodynamic conditions and time of the etching [34, 35, 36, 37]. In accordance to the literature, the overall ion-exchange between the Li^+/H^+ ions led to the cubic niobium acid (*c*-$HNbO_3$) (see Figure 6) [36]. In the literature, a model of crystalline structure of the exchanged layer after proton exchanged reaction was presented (see Figure 7). The lithium ions were substituted by the hydrogen ions but not in the exact atomic position, the hydrogen ions were placed in the anti-site location. These differences in the ions position led to changes of the crystal structure of the $H_xLi_{1-x}NbO_3$ [25]. The obtained structure was centrosymmetric and non-ferroelectric [38]. Because of the ions exchange the new crystalline structure on the surface was deformed and a strain was present between the surface exchange and the deep bulk $LiNbO_3$ layers. Since the $LiNbO_3$ was photo-elastic and piezoelectric, the strain inside the crystal induced an electric field that, through the electro-optic effect, caused local variation of the refractive index. In addition, the presence of this internal electric field could induce spontaneous domains inversion at the $H_xLi_{1-x}NbO_3$:$LiNbO_3$ interface [29]. From former work, it was recognized that ion substitution could be conducted in an environment of the organic or inorganic solution. It is well known that an inorganic ion-exchangers generally have superior selectivity to those of the ordinary organic ion-exchangers without any special treatment such as chelation, especially in the separation between ions in similar groups such as alkali metal ions, divalent ions, and trivalent ions [35].

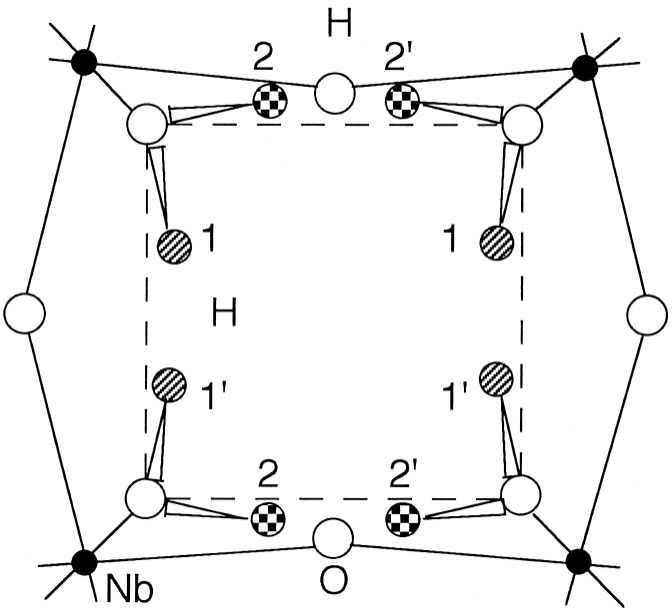

FIG. 6 Atomic position of the *c*-$HNbO_3$ lattice [36].

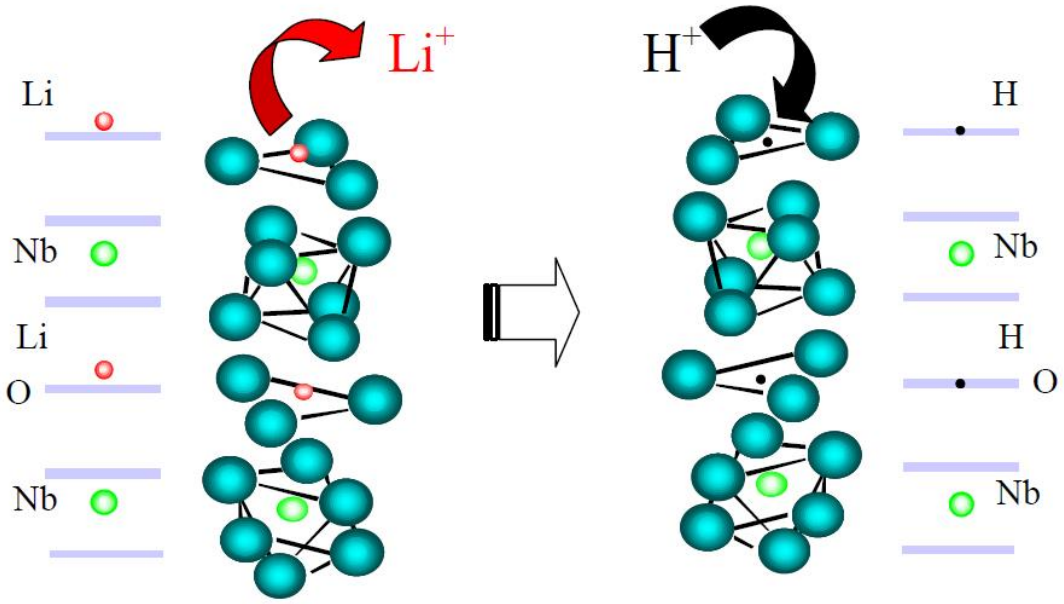

FIG. 7 Crystalline structure of the $LiNbO_3$ modified by proton exchanged reaction [39].

1.6 Crystal's growth

1.6.1 Czochralski's technique

$LiNbO_3$ crystals were grown with Czochralski's technique (see Figure 8). The seed of the crystal is introduced to the melt of congruent substrates of the lithium niobate that begins the crystal growth. Next, crystal is pulling up, to the final form of the crystal boule.

Usually, the congruent lithium niobate crystals are grown along the polar *z*-axis (so-called 0°-crystals). The $LiNbO_3$ crystal has the mirror planes *outcrop* on the cylindrical boule surface as three clear facets aligned along the growth axis [14]. The congruent samples are formed from lithium carbonate and niobium pentoxide, with ratio 48.6 % mol Li_2CO_3:51.4 % mol Nb_2O_5. The chemical formula for crystal growth is given by the reaction:

$$Li_2CO_3 + Nb_2O_5 \rightarrow 2LiNbO_3 + CO_2 \tag{6}$$

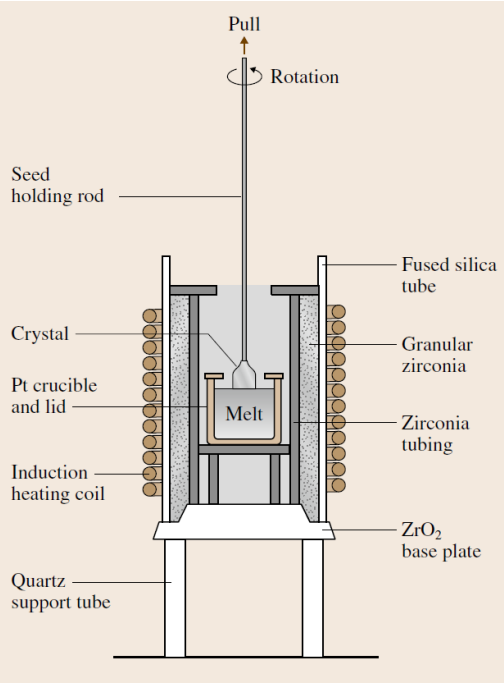

FIG. 8 A basic diagram of the Czochralski's method [22].

FIG. 9 $LiNbO_3$ single crystal with diameter corresponds to 2-inch wafer. Crystal is oriented to the *z*-axis. Picture made on crystal prepared in Institute of the Electronic Materials Technology (ITME laboratory).

1.6.2 Congruent $LiNbO_3$

$LiNbO_3$ shows a tendency to form congruent crystals. The actual chemical composition is related to the quantity of the lithium oxide content in the starting mixture, equal to 48.4–48.6 mol % of Li_2O (see Figure 10). The ratio of the lithium (Li_2CO_3) to niobium (Nb_2O_5) substrates, which are introduced to the melt, correspond to the actual composition of the crystal sample with the ratio of the [Li]/[Nb]=0.94 [40]. The Li deficiency in the $LiNbO_3$ corresponds to the Li–O bonds, which are weaker than the O–O and Nb–O bonds. Therefore, lithium niobate is a material, which contains, usually a high concentration of the lithium vacancies, $V_{Li}^{'}$ and much lower concentration of the niobium vacancies, $V_{Nb}^{5'}$, because the highly charged $V_{Nb}^{5'}$ vacancies appear to be energetically unfavourable [1, 41].

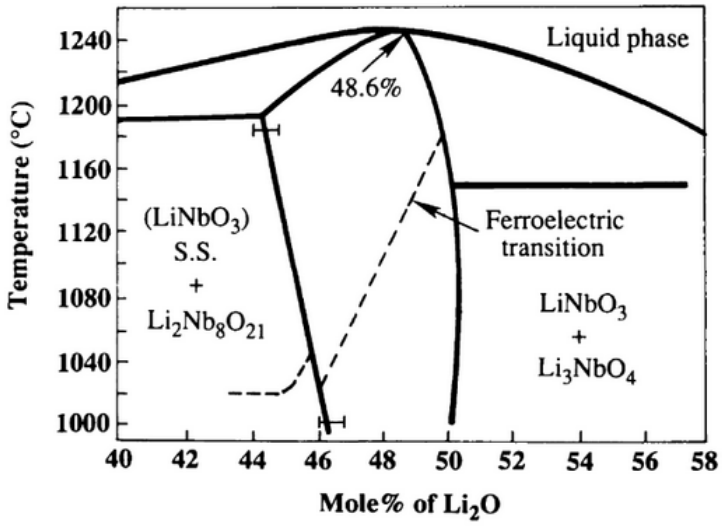

FIG. 10 The phase diagram of Li_2O-Nb_2O_5 system [42].

1.7 Defects in $LiNbO_3$

The extended defects play an important role in a transport processes. The easy diffusion paths facilitate the migration of the ions. The surface layer of the crystal is a special example of the extended defect [43]. The occurrence of the inhomogeneous surface, which shows a disturbed spatial distribution of the ions, in a wide range of the concentrations, was reported recently for the strontium titanate [11]. Such a disturbed surface occurs in the double oxide materials. The description of the surface layer quality is important from technological point of view [44].

Defects in the lithium niobate were described in literature from the experimental point of view [49, 45] and theoretical calculation [16, 41]. There are models proposed in literature [16, 46, 47, 48], which describe the shortage of the Li during the growth. The models correlate the occurrence of the Li, Nb, and O vacancies, however, the structural measurement and theoretical calculations show low probability of the existence of oxygen vacancies in *as–grown* crystals, as shown in the paper by Donnerberg [16]:

$$LiNbO_3 \longrightarrow Li_2O + 2V_{Li}^{'} + V_O^{2\bullet}. \qquad (7)$$

Deficiency of the Li ions induced during the crystal growth were described by several formulas, defining Li_2O out-diffusion and variance in created defects:

$$LiNbO_3 \longrightarrow 3Li_2O + 4V_{Li}^{'} + Nb_{Li}^{4\bullet}, \qquad (8)$$

$$LiNbO_3 \longrightarrow 3Li_2O + 4V_{Nb}^{5'} + 5Nb_{Li}^{4\bullet}, \qquad (9)$$

$$LiNbO_3 \longrightarrow 3Li_2O + 4(Nb_{Li}^{4\bullet} - V_{Nb}^{5'}) + Nb_{Li}^{4\bullet} \qquad (10)$$

The energetically most favourable (4.56 eV) is the mechanism (8), where the occurred Li vacancies are compensated by the Nb antisites. Less favourable is the process (10) which needs energy of the 10.67 eV, and the least probable is the mechanism (9) with 15.17 eV. The occurrence of such defects is verified with the use of the diffraction experiments.

It is well known that the crystal structures of the ilmenite ($FeTiO_3$) and lithium niobate are very similar, and differ only by their cation stacking sequences. Donnerberg *et al*. [16] have shown, with the use of the computer simulation, that lattice energy per unit cell of the ilmenite is only 0.1 eV less favourable than the respective energy for perfect $LiNbO_3$.

Intermixing of both structures in the $LiNbO_3$ can be possible. Experimental evidence of this theory was given by Kumada *et al*. [49].

Hence, the congruency occurs due to the crystal growth conditions. However, it can be also modified due to higher affinity of the lithium cations than that of niobium cations, combined with purposeful thermal gradients, applied to the crystal samples. Changes in chemical composition would be dominated by the Li cations mobility [50].

For crystals modified in reduction conditions the model for structural defects for congruent lithium niobate was proposed [16, 51]:

$$3O_O + 2V_{Li}^{'} + Nb_{Nb} \leftrightarrow \frac{3}{2}O_2 \uparrow + Nb_{Li}^{4\bullet} + 6e^- \qquad (11)$$

According to the model (eq. 11), loss of oxygen from the lithium niobate surface is correlated with an incorporation of the left Nb^{5+} ion into the empty Li site and consecutively to a total redistribution of the V_{Li} and Nb_{Li}. Created electrons are trapped by Nb ions. Oxygen vacancies do not appear because the released electrons are captured by traps after oxygen leaves the crystal surface.

1.8 Easy diffusion path

It is deduced that migration of the ions or atoms in the crystals with dislocations can be more rapid in vicinity of the dislocation lines than through the lattice (matrix). This behaviour is a consequence of "a loosening up" of the crystallographic structure along the dislocation line. The breaking of the translation symmetry is a result of the increase of the interatomic distance along the dislocations line, which allows a more effective transport of atoms or ions. This enhancement of the diffusivity is termed pipe diffusion. The total diffusion in the crystals is the sum of the regular lattice diffusion and the pipe diffusion, which depends on the density of the dislocations and the radius of the effective region around the core of the dislocations (pipe) [11]. With accordance to Harrison's classification, who described, the diffusion in the medium with extended defects into three kinetic regimes (see Figure 11) [52]:

1. Type A kinetic

   $\sqrt{Dt} > \Lambda$,

   where D is the diffusion constant, t is time, and Λ is the average distance between dislocations. For this type of kinetic regime, it is observed an overlap of the diffusion fields of neighbouring dislocations.

2. Type B

   $a \ll \sqrt{Dt} \ll \Lambda$,

   where a is the pipe radius.

3. Type C

   $a > \sqrt{Dt}$.

   It is a pipe diffusion; the diffusion process dominates along the core of dislocation.

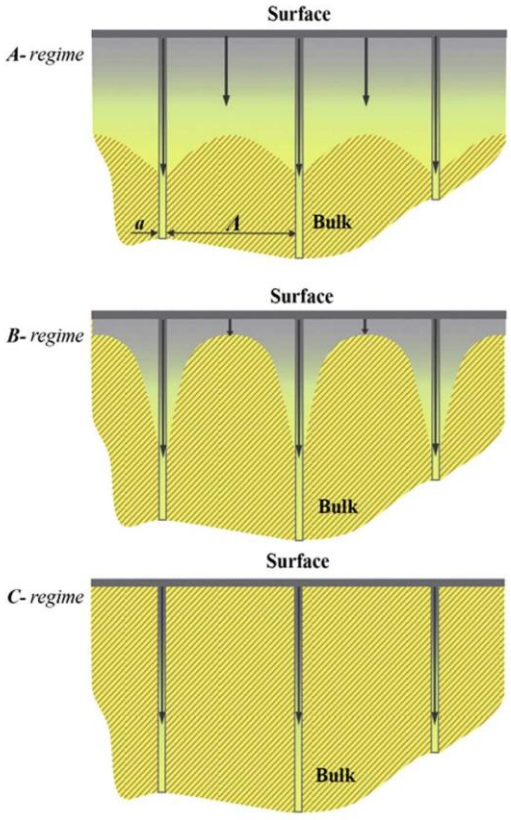

FIG. 11 Three regimes of diffusion along the short –circuiting paths proposed by Harrison [52].

2 Experimental

2.1 $LiNbO_3$ samples

The $LiNbO_3$ single crystals were delivered from CrysTec GmbH (Berlin, Germany) and from Institute of the Electronic Materials Technology (ITME) laboratory (Warsaw, Poland). All used crystals were grown by Czochralski's technique, from the congruent melt. Crystals delivered from CrysTec GmbH were oriented in respect to the polar *c*-axis (*z*-cut, $(0001)_k$ direction) with dimension $10\times10\times1$ mm^3 and dimension $10\times10\times0.5$ mm^3. The symmetry of both crystals was checked with XRD test. Symmetry *R3c* of $LiNbO_3$ at room temperature was confirmed. The *as-grown* samples of the $LiNbO_3$ crystals had epi-polished surfaces. Samples for all measurements were cut to demanded dimensions. Prepared samples have been taken for proton exchange reaction, then the modified crystals were analysed with TOF-SIMS technique and Brillouin spectroscopy. Pure $LiNbO_3$ crystal samples and crystals modified with reduction conditions were used to the following measurements: XPS, ICP-OES, TGA, effusion mass spectrometry, and TOF-SIMS measurements.

The crystal obtained from ITME laboratory was oriented to the polar x-axis. Crystal sample was grounded in agate mortar, and sieved. Size of the crystal grains, used for experiment, was bigger than 70 μm. The powdered crystalline samples were used for leaching and etching procedures. The crystalline powder of the reference sample (pure, congruent) and samples modified by the leaching reactions were taken for the following measurements: ICP-OES, XRD, and electrical measurement.

2.2 Proton exchange

Proton exchange process is a mechanism which leads to substitution of one ion, with another. Proton exchange reaction corresponds to the lithium niobate crystal leads to substitution of the constituent lithium ions, by hydrogen ions provided from the liquid solution into the lithium sublattice. In our experiment, the chemical reaction was conducted in environment of the concentrated nitric acid at increased temperature. Proton exchange process is given by following reaction [36]:

$$LiNbO_3 + xH^+ \leftrightarrow H_xLi_{1-x}NbO_3 + xLi^+ \quad (12)$$

2.2.1 Conditions of chemical reaction

The proton exchange reaction was carried out at two kinds of measured samples: as-received crystals and powdered crystalline samples. The parallelepiped samples of crystals were cut-off, with use of a diamond-wire saw. Samples with dimensions about 2.5×3.5×0.5 mm^3 were taken to the experiment (see Figure 12). The other samples were prepared from the crystal which was grounded in agate mortar, and sieved (see Figure 13). Size of the crystalline grains, used for experiment, was bigger than 70 μm.

Proton exchange reaction Li^+/H^+ was conducted in an environment of the concentrated nitric acid HNO_3(V) (65%, puriss p.a.). The HNO_3(V) acid was poured into the 250 ml flask equipped with a reflux (see Figure 16).

Crystal samples of the $LiNbO_3$ were dropped at once into the flask, and reaction was conducted at the stabilized temperature equal to 110±3 °C. Additional 60 ml portions of 65% nitric acid were added in 24 hours intervals subsequently to sustain the same concentration of the H^+ ions. The reference crystal sample was etched for 1 hour in HNO_3. Short etching time was applied to the purification of the surface of the crystal sample. After 120, 240, and 480 hours part of the samples of the lithium niobate were removed from the flask, to break the chemical reaction, and rinsed in the ethyl alcohol [53].

FIG. 12 Lithium niobate crystal samples with epi-polished surface.

Similar chemical conditions were maintained for the powdered crystalline sample. The powder was put into the flask. Reaction was carried out at the stabilized temperature equal to 80±3 °C. Portion on pure concentrated nitric acid (50 ml) was added in 24 hours intervals to sustain the same concentration of the H^+ ions. After 48 hours the powder sample was removed from the flask, the chemical reaction was stopped and protonized powder sample was rinsed in the ethyl alcohol [54].

FIG. 13 Powdered crystalline lithium niobate and powdered sample in liquid solution.

2.2.2 Proton exchange setup

An integrated setup of laboratory apparatus was made especially for carrying out the proton exchange (PE) reaction in the $LiNbO_3$ crystals. The environment of the reaction was the concentrated inorganic acid nitric acid (HNO_3 65 %, puriss p.a.). The apparatus allowed to conduct the PE reaction on various crystals in different environment of the inorganic acids at the concentrated and diluted solution. Created set-up provided a safe and convenient scientific experiment for long-term processing. The apparatus setup (see Figures 17 and 18) enabled us to avoiding any life threatening with reaction conducted in tough environment of concentrated acid. The set-up is composed of multiple parts, which are suitably arranged to an entity, *e.g.*, flask, Allihna cooler, distillation cooler, distillation flask. The novelty is conjunction of tubes and taps, which combines two chemical configurations at the same time. This improvement allows switching the radiator from the callback to the flow (and *vice versa*) at any time. The use of the appropriate string of glass bubbles inside the tube is significant for reflux efficiency in the apparatus setup. The setup had part of apparatus responsible for distillation process necessary for made a subsequent exchange of proton donor (*e.g.* nitric acid). Materials used to produce the setup as well as reagents such as nitric acid, which is the main source of the protons, are inexpensive. The setup for proton exchange reaction was patented, and the title is: "*Apparatus for carrying out protonated crystals in solutions of inorganic acids, has flask connected to thermometer and tube through second tap, which includes radiator, and adapter connected with radiator and receiver*", Patent Number: PL406671-A1, Patent Assignee: UNIV SLASKI, authors: Irena Gruszka, Andrzej Molak and Julita Piecha.

FIG. 14 Picture of the reaction flask with tubes and tap.

FIG. 15 Picture of the conjunction of tubes and tap.

FIG. 16 Picture of reaction flask with samples placed in to the beaker with methyl silicone oil.

FIG. 17 Picture of setup for proton exchange reaction.

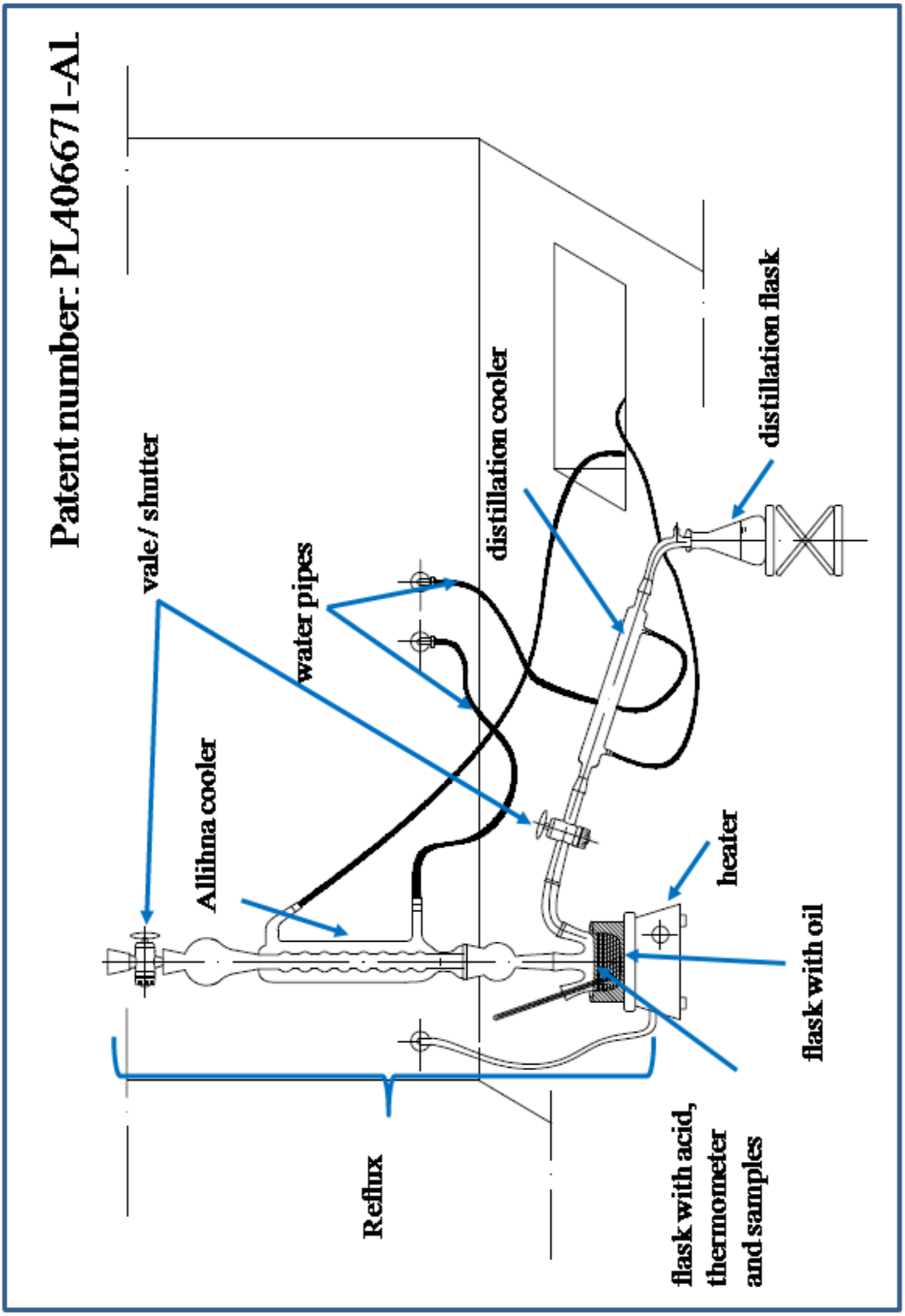

FIG. 18 Setup for proton exchange reaction.

2.3 Methods

2.3.1 Time of flight secondary ion mass spectroscopy (TOF-SIMS)

The SIMS is the microanalytical method that allows to observe charged particles, *i.e.*, secondary ions, ejected from the surface of the sample after the studied material surface, bombarded by primary beam of heavy particles. This technique is used to determine of the, *e.g.*, isotopic, elemental, molecular composition of studied material. The method enables to study a surface of the solid materials, interfaces between chemically different solids, and internal part of the material volume [55].

Obtained depth profiles and chemical composition of the lithium niobate surface layer was carried out with using VG SIMSLAB apparatus. The measurements were conducted under UHV conditions (p=10^{-11} bar). The lateral resolution was in the range of the 0.1–3 μm [56]. The characterizations of the measured conditions were presented below.

The depth profiles of the H, Li, Nb, and O_2 ions were obtained for a reference sample and for the crystal samples etched for 240 and 480 hours, at the room temperature. The setup was equipped with Cs sputter source gun, with energy beam equalled to 2 keV and current ~130 nA, the etching area was ~300×300 μm^2. The primary Bi source had the energy beam equalled to 25 keV at the ion current of ~0.9 pA, the analysis area was equal to: ~80×80 μm^2.

The morphology maps were obtained with use of static SIMS. Analyses were conducted on the crystal samples, which were reduced *ex situ* in 0.5 bar atmosphere of deuterium for 2 hours, at temperature conditions stabilized at the 750, 850, and 950 °C. It should be noted that deuterium gas was used to reduce the samples. The use of deuterium enabled us to omit ambiguities related to a possibility of embedding flowing gas ions in the crystal lattice. The matrix effect was minimised with use of the renormalization of the data, *i.e.*, the ratio [Li]/[Nb] was estimated. The TOF-SIMS setup was employed with Cs sputter source gun, with energy beam equalled to 1 keV and current ~88 nA, the etching area was ~300×300 μm^2 and primary Bi source of energy beam equalled to 25 keV at the ion current of ~0.8 pA, the analysis area: ~80×80 μm^2.

2.3.2 X-ray diffraction (XRD)

The X-ray diffraction measurement allows to identify the crystallographic structure of the powdered samples.

The powdered crystalline sample of the $LiNbO_3$ was studied with the use of an X-ray powder diffractometer SIEMENS Kristalloflex-4 using filtered CuK_α radiation (λ=0.154056 nm; U=25 kV; I=15 mA) and the θ–θ scan technique. The diffraction pattern was collected in the 2θ range (20º–100º) with scan step 0.02º and the time count was 39 s for each point, at room temperature equal $T\approx300$ K. The intensity and position of each measured line was fitted using the least–squares method by means of a computer program called the X–ray Reflection Profiler [57]. The processes of the crystal structure refinement were performed using the profile Rietveld method by means of the FullProf software [58]. XRD analysis has shown the rhombohedral structure with the space group *R3c* for measured samples [59].

2.3.3 Inductively coupled plasma-optical emission spectroscopy (ICP-OES)

The concentration of the lithium and niobium in liquid solutions was determined by using an optical emission spectrometry with excitation by the argon inductively coupled plasma (SPECTROBLUE ICP-OES, Spectro Analytical Instruments, Germany). External calibration was performed with the standards prepared quantitatively by dilution of the Merck Certipur® (Li) and Sigma-AldrichTraceCERT® (Nb) certified plasma emission standards with water. The concentration of the lithium and niobium ions was estimated from the emission lines of the Li 670.780 nm and Nb 309.418 nm. The optimum measurement conditions were shown in Table 1. The total content of analytes in samples leached with redistilled water and nitric acid 65% were tested.

TABLE 1 Measurement conditions for ICP-OES.

Rf power, kW	1.4
Frequency, MHz	27.12
Plasma torch	quartz

Plasma gas flow, L min^{-1}	14.0
Auxiliary gas flow, L min^{-1}	1.0
Nebulizer gas flow, L min^{-1}	1.0
Cross flow nebulizer, bar	2.4
Scope of the polychromator, nm	165-285 / 285-470
Holographic grid, grooves mm^{-1}	3600 / 1800
Sample uptake, mL min^{-1}	1
Exposure time, s	3
Number of replicates, s	3

2.3.4 Electrical measurement

The electrical measurements were performed with the use of the Wayne Kerr 4300 LCR meter and the Unipan 680 temperature controller. The powdered crystalline samples were placed in a cylindrical teflon tube-holder, with inner diameter of the 3.15 mm. The cylindrical piston was inserted from the top to the teflon tube. The bottom electrode and the top piston (bottom surface) were painted with the Ag paste. The powder samples were pressed with the axial pressure of 5 bar. The measurements were conducted in the heating and cooling cycles at the temperature range from 300 K to 650 K, with heating and cooling rate of the 1.5 K min^{-1}. The spectra were obtained for frequencies from the range of 20 Hz to 1 MHz, all powdered samples measurements were repeated several times. The capacitance, *C,* conductance, *G,* and dc resistivity, *R,* were measured and the effective electric permittivity, ε_{eff}, the loss coefficient, $tan\delta$, and conductivity, σ, were calculated.

2.3.5 Brillouin Scattering

The Brillouin measurement was conducted with using a conventional tandem multi-pass Fabry-Perot interferometer (TFP-1, JRS Co.). For as an excitation source was used a diode-pumped solid-state laser (Excelsior 532-300, Spectra Physics) at a wavelength of 532 nm.

The signal was detected and averaged with the use of the conventional photon-counting system combined with a multichannel analyser. The Brillouin spectrum was obtained for 1024 channels after a few hundreds repetitions of accumulation with a gate time 500 ms for one channel. For temperature variation was used a high-temperature cell (TSI500, Linkam). More details about experimental apparatus was described in paper [60, 61].

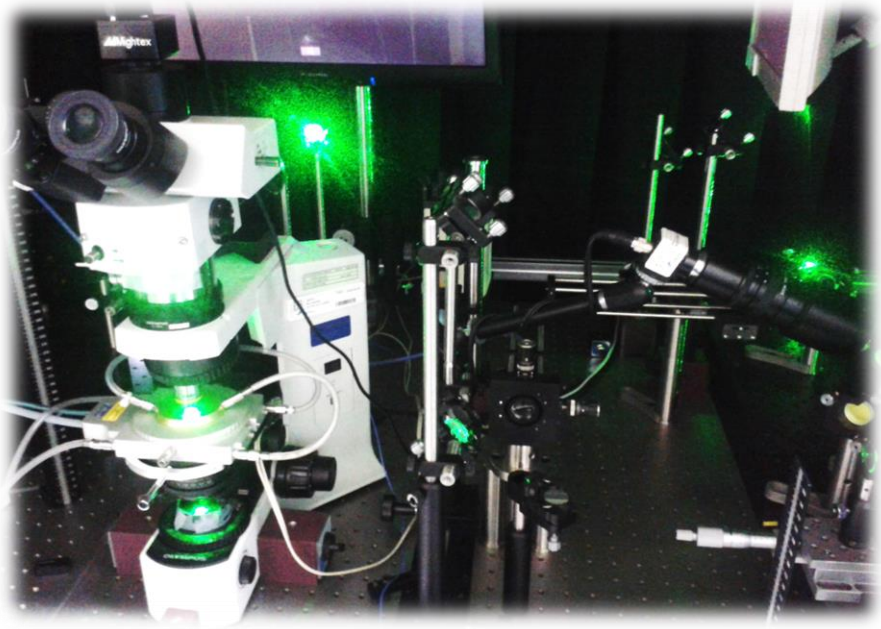

FIG. 19 Apparatus for Brillouin spectroscopy with high-temperature cell.

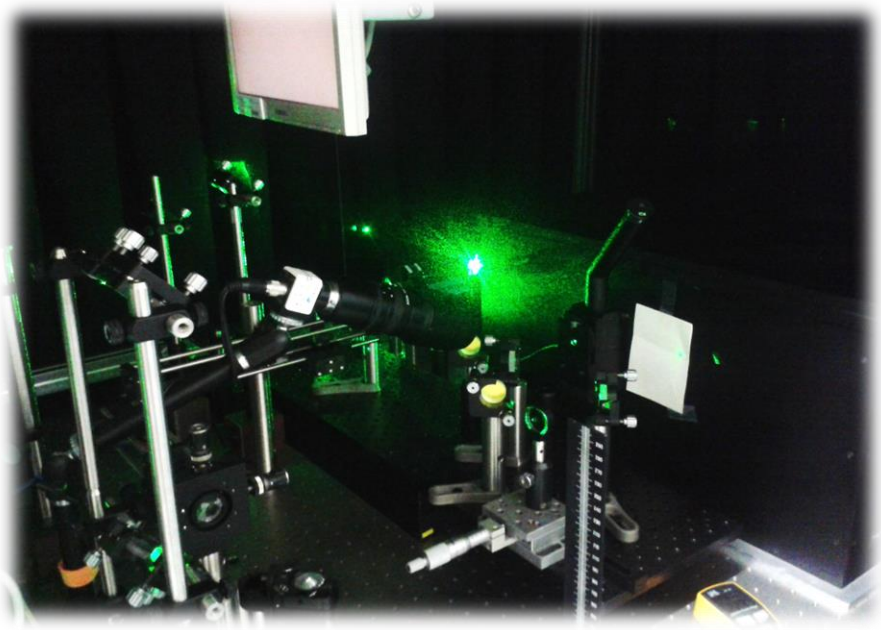

FIG. 20 Apparatus for Brillouin spectroscopy with optical setup.

2.3.6 X-ray photoelectron spectroscopy (XPS)

The XPS, sensitive method allowed obtaining information about composition and concentration of the elements from near-surface (~6 nm) area. The XPS analysis was conducted on Physical Electronics PHI 5600 spectrometer. The spectrometer used the Al K_α monochromatic X–ray source for the excitation with the energy of 1486.6 eV. The measurements were carried out at take–off angle equal to 45˚, that provided the test depth of about 6 nm. Photoelectron spectra were calibrated against the peaks of Au 4f7/2 at 83.98 eV, Ag 3d5/2 at 368.27 eV, and Cu 2p3/2 at 932.67 eV of binding energy. The electron gun was used for the compensation of positive surface charge, which may appear on the insulator ferroelectric surface. The XPS measurements ware conducted in the temperature range of 300–900 °C in situ for the core lines of the Li 1s, Nb 4s, Nb 3d, O 1s, C 1s, and the valence band. The core line spectra were recorded: *in situ*, in ultrahigh vacuum of 10^{-12} bar, from an area of 1.6 mm in diameter, and with resolution of 0.1 eV.

2.3.7 Thermogravimetry (TGA)

TGA tests were carried out with use of a Netzsch TG 439–type thermo–balance apparatus. The materials were placed in the platinum crucible vessel. The oxygen partial pressure was lowered to 10^{-23} bar, and measured with the use of the lambda probe. When the high temperature range was reached, the oven chamber was filled with a gas mixture. The samples were annealed under reduction and oxidation conditions. The mass change was determined in the temperature range of the 500–1000 °C. The temperature was increased to 100 °C steps, and each step was stabilized for 4 hours. The reduction reaction was carried out in the gaseous mixture of 96% Ar + 4% H_2 at the pressure equal to 1 bar. TGA was carried out on four samples: *as-received* epi-polished crystal, *as-received* with rough surface crystal, powder with mean diameter of ~85.00 μm, and fine powder with mean diameter of ~25.08 μm. The mass of the samples taken for this experiment was: ~44.44 mg for crystals, 44.73 mg for powder, and 44.57 mg for fine powder. It was noticed that the reduction of crystals induced the non–transparency of samples (see Figure 21). The oxidation reaction was carried out in the mixture of 79% Ar + 21% O_2 at the pressure equal to 1 bar. The mass of crystal sample taken for this experiment was 35.80 mg.

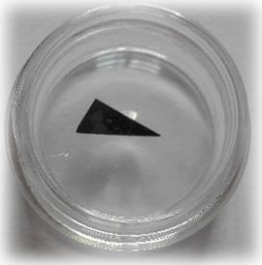

FIG. 21 Lithium niobate crystal after reduction.

2.3.8 Effusion

Effusion test lead to identification of the gasses released from the crystal sample. The lithium niobate crystal was placed to effusion chamber equipped *inter alia* with heater and quadrupole mass spectrometer (see Figure 22).

Effusion processes were conducted under UHV (p=10^{-12} bar) conditions, on the ferroelectric crystal platelet samples with the dimensions of the 10×10×0.5 mm^3. Tests were carried out at the T=800 °C and T=900 °C, *i.e.,* thermal treatment was applied for one hour per each measurement. Components released from the surface layer of the crystal were detected and identified by using a mass spectrometer.

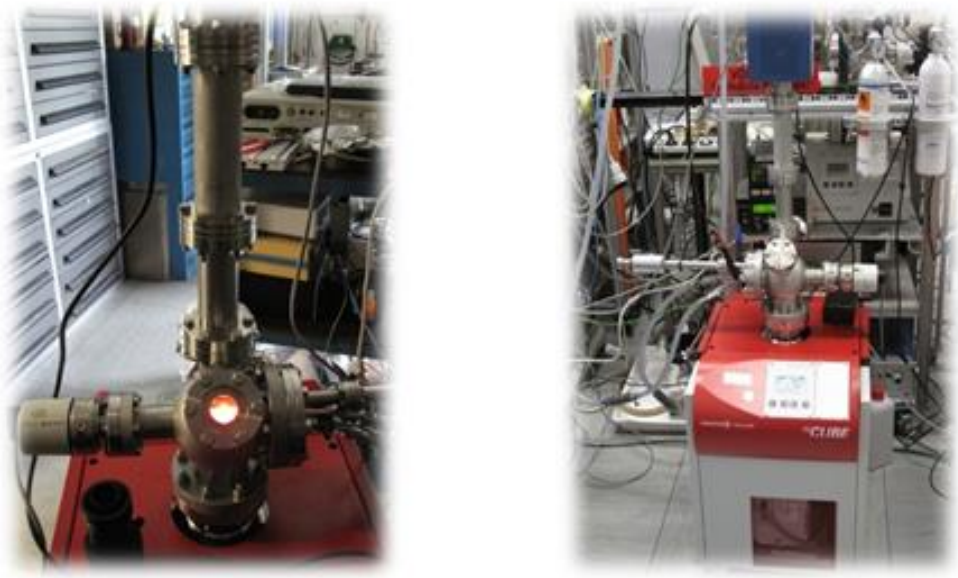

FIG. 22 Apparatus for effusion measurement. The effusion chamber with heater and mass spectrometer.

3 Results and discussion

3.1 Proton exchange (PE) effect

First aspect of my work was concentrated on influence of the PE reaction on the lithium niobate samples. It was important to define changes in the surface layer obtained by the chemical reaction and to check how the modified layer could behave in comparison to the whole volume of the crystal.

3.1.1 Ions substitution

The TOF-SIMS analysis was carried out to check the level of ions substitution Li^+/H^+ in the protonized samples in the environment of concentred nitric acid and to try whether proton exchange reaction would provide modification of the surface crystal sample. Depth profile was obtained to verify possible substitution of the matrix ions.

Figure 23 showed value of the normalized intensities of the ions. They were obtained for pure (reference) $LiNbO_3$ sample and for samples etched in the nitric acid during 240 h and 480 h of time reaction.

The reference sample (etched during 1h to remove the residual contamination) showed flat profiles, which indicated uniformed distribution of the ions within the surface layer. It is worth to note that etched samples (for 240 and 480 h) exhibited changes which occurred for H profile at ~250 and 380 nm, respectively. The intensity dropped sharply about one order of magnitude. On contrary, a gradual increase of the normalized intensity, followed by a sharp rise, was observed for Li ion profile. The O_2 profile showed also changes in the intensity. We deduced that lithium ions were removed from the crystal in the form of the lithium oxide. The proton exchange region extended from the crystal surface to interior part of the crystal sample to the depth ~250-380 nm. The complementary feature of the H and Li concentration profiles confirmed that the proton exchange reaction took place. The $H_xLi_{1-x}NbO_3$ crystal structure was formed. In accordance to the SIMS test mentioned results, the deeper part of the sample, *i.e.* below ~380 nm, showed the intact nominal composition of the $LiNbO_3$. The relatively constant Nb profile was consistent with the deduction that the Nb sublattice remained intact. The exchange reaction, which occurred between H^+ and Li^+ ions, was confirmed by the ICP-OES measurement.

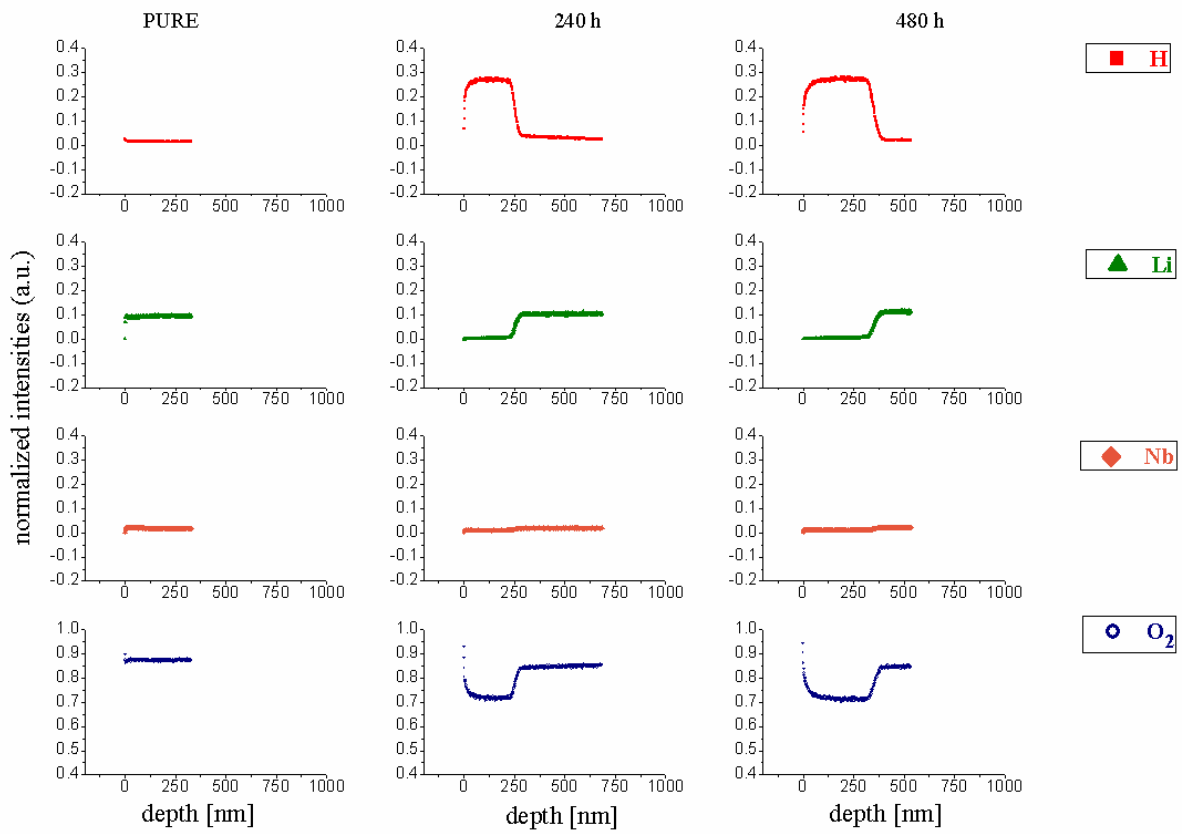

FIG. 23 Depth profiles of the H, Li, Nb, and O_2 ions obtained from SIMS, for pure and etched for 240 and 480 hours samples.

3.1.2 Solvent analysis

The differences that occurred from the depth profiles obtained from the SIMS data were motivation to perform analysis solvent from the PE reaction. The concentration of the lithium and niobium ions in the liquid solution was analysed with using the ICE-OES apparatus. Measurements were performed after the powdered samples were leached. For powder samples leached in the redistilled water and for samples leached in the concentrated nitric acid the emission of the lines Li 670.780 nm and Nb 309.418 nm in radial view was evaluated. No Li and Nb ions were detected in the blank reaction. The emission of main lines values and the weight of the solution were used to estimate the total content of the leached elements. A total concentration 48.67 µmol = 337.8 µg of the Li and 15.99 µmol = 1486 µg of the Nb was found in the redistilled water solvent. A total value of the Li 1261 µmol = 8754 µg and 0.18 µmol = 17.12 µg of the Nb ions was exhibited for nitric acid solvent. For both used solvents, the concentration of the lithium ions was higher than the concentration

of the niobium ions. It is worth to notice that environment of the redistilled water was more favourable for transfer of the niobium ions (from the sample to the solvent) than environment of the concentrated nitric acid. Furthermore, the concentration of the lithium in nitric acid was two orders of magnitude higher than the value estimated for the redistilled water.

According to the depth profiles obtained from SIMS measurements for the lithium niobate crystal samples, modified by proton exchanged reaction carried out in the environment of the concentrated nitric acid, it was observed that lithium ions were substituted with the hydrogen ions. It was deduced that ions replacement of the Li^+/H^+ provided charge compensation in the $H_xLi_{1-x}NbO_3$. In case of this effect, the niobium ions could not migrate from the sample to the liquid solvent.

3.1.3 Structural modification

The unexpected result, from the chemical point of view, obtained from the ICP-OES measurement, which showed lower concentration of the niobium ions in nitric acid solution than in redistilled water, was explained in accordance to the structural changes in the lithium niobate. The analysis was carried out with using the XRD technique. For pure lithium niobate, the rhombohedral crystallographic structure with the *R3c* symmetry was confirmed (see Figure 24 and Table 2).

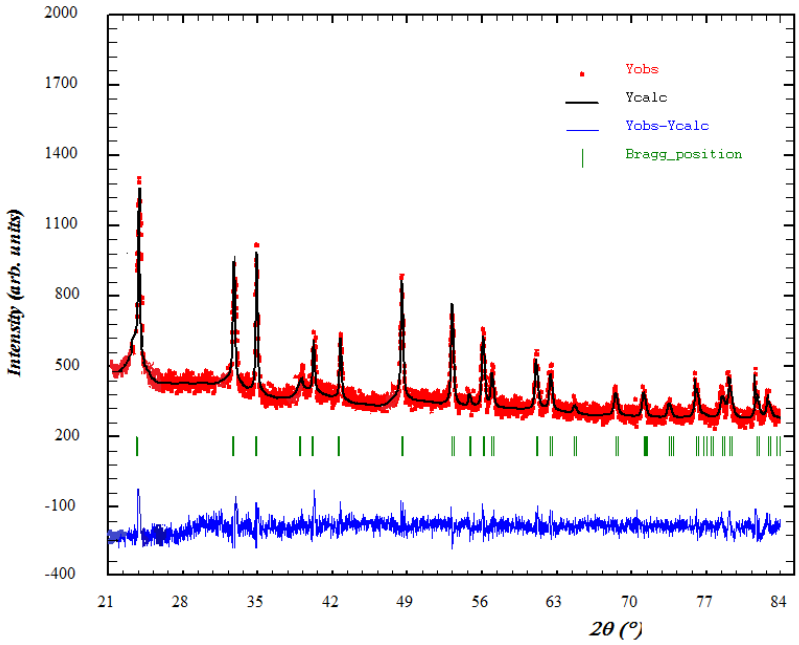

FIG. 24. Refined X-ray powder profile obtained for the $LiNbO_3$.

TABLE 2 Results of the Rietveld refinements conducted for the $LiNbO_3$.

Space group: *R3c* (*No. 161*); Lattice constants: a=5.1513(9) (Å); c=13.8739(9) (Å); R_{Bragg}=10.65%				
Atom	x	y	z	B^{iso} [Å]^2
Li (6a)	0.0000	0.0000	0.3421(9)	1.6271(8)
Nb (6a)	0.0000	0.0000	0.0258(3)	1.0412(7)
O1 (18b)	0.0658(9)	0.3612(7)	0.0945(4)	1.8423(4)

The XRD pattern lines obtained from the measurements performed for reference and leached powdered crystalline samples were shown in Figure 25. Leaching reaction conducted in the redistilled water solvent changed slightly shape of several lines in the patterns (compare Figure 25(a) and 25(b)). The main Bragg peak, visible in vicinity of 27 [deg], included an additional component. This effect could be correlated with the stress-strain effect and also with non-homogenous distribution of the elements in the surface of the powdered sample caused by the leaching reaction. However, the number of the pattern lines did not change. Hence, occurrence of the intact set of the lines indicated that the crystallographic structure of the lithium niobate was maintained. On the other hand, the intensity of this pattern lines, obtained for the sample leached at the redistilled water, was significantly lower than the intensity obtained for the reference powder. The intensity decrease was assigned to the deficiency of the atoms in the crystal lattice. It is worth to note that these changes in the pattern line corresponded to the result obtained from ICP-OES analysis in accordance with the lithium and niobium ions released from the powdered sample to the liquid solvent.

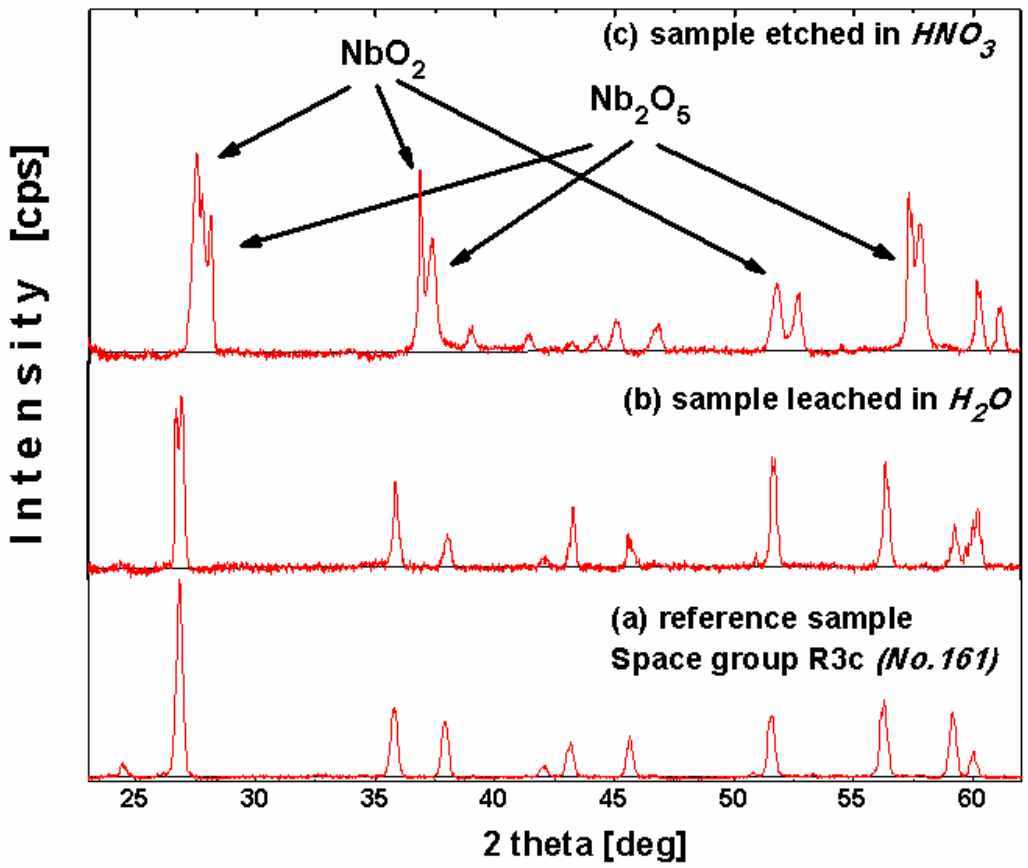

FIG. 25 The XRD pattern obtained at the room temperature for crystalline powder samples of the $LiNbO_3$: (a) reference, (b) leached in the redistilled water, and (c) leached in the nitric acid.

The marked change in the pattern line was detected for the powdered sample leached in the concentrated nitric acid (see Figure 25(c)). One could distinguish a set of reflections in the XRD pattern, which corresponded to the distorted structure of the defected lithium niobate, It was also noted the fitting to the *R3c* symmetry failed. The actual crystal structure showed monoclinic symmetry (see Figure 26). The additional reflections in the pattern could be assigned to the Nb_2O_5 and NbO_2 oxides precipitation. Their occurrence resulted from leaching process when the Li ions migrated to the solvent. One could not exclude that the NbO_2 species corresponded to the Nb-O subsystem, which remained after lithium ions were released. In accordance to the literature, the overall ion exchange between the Li^+/H^+ ions led to the cubic niobium acid (*c*-$HNbO_3$) [36]. Longer time of the protonization could have led to the structural modification from rhombohedral to cubic.

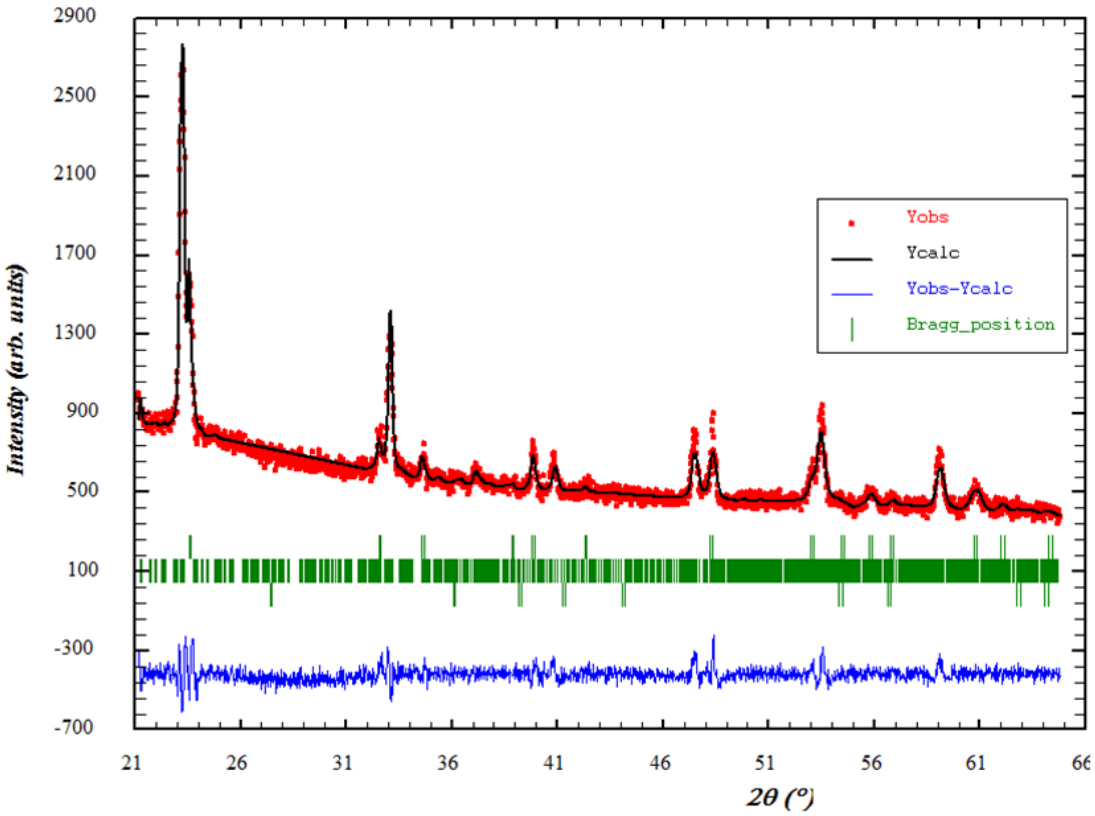

FIG. 26 Refined X-ray powder profile obtained for the $LiNbO_3$ modified by proton exchange reaction.

The higher noise in the background line was observed for both modified by the leaching reaction samples. The signal to noise (S/N) ratio was lower than the ratio for the referenced sample. The differences of the S/N ratio could be explained in accordance with the effect of non-homogeneity induced by the chemical reaction. It was noticed that structural features of the surface of the powders, modified by the leaching reaction, corresponded to the generation of an amorphous layer.

3.1.4 Electrical features

The influence of the PE was confirmed with the SIMS, ICP-OES and XRD tests. The XRD volumetric method of the structure determination showed that PE induced new crystal structure. Next step was to correlate electrical features of the prepared samples. It was expected that PE reaction could induce electrical non-homogeneity.

The measurements were conducted to identify the differences in the electric permittivity ε_{eff}, the loss coefficient *tanδ,* and conductivity σ induced by the leaching procedure. Figure 27 showed electric permittivity ε_{eff} *vs*. temperature *T* dependencies for the reference and the leached samples. For the reference sample (Figure 27(a)) the dispersion increased from the range 380K to 650K. For both leached powdered samples (Figure 27(b) and 27(c)) we observed a marked dispersion in wider range of temperature. The anomaly was observed at the low frequency range (marked A in Figure 27). The shape of the anomaly changed, decreased after leaching in the redistilled water and almost vanished after leaching in the nitric acid.

The dielectric loss coefficient *tanδ vs*. *T* was shown in Figure 28. The marked frequency dispersion in the whole temperature range was notice for all measured samples. For pure samples leached in the redistilled water, it could be observed an anomaly with one minimum in vicinity of the temperature 390K. For sample leached in the acid, there was a double anomaly with minimums at the 350K and 500K.

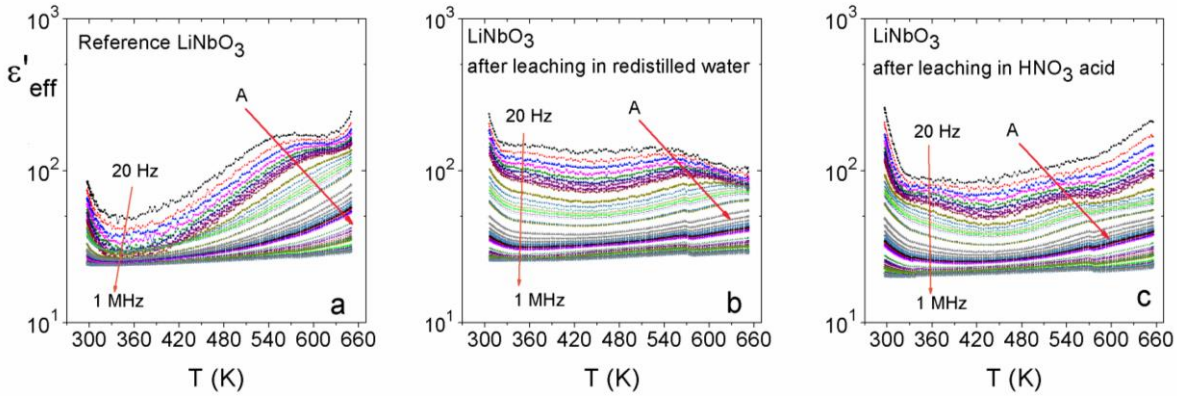

FIG. 27 The dielectric permittivity ε_{eff} *vs.* temperature *T* dependencies. Measurements were carried out for crystalline powder samples of the $LiNbO_3$: (a) reference, (b) leached in the redistilled water, and (c) leached in the nitric acid.

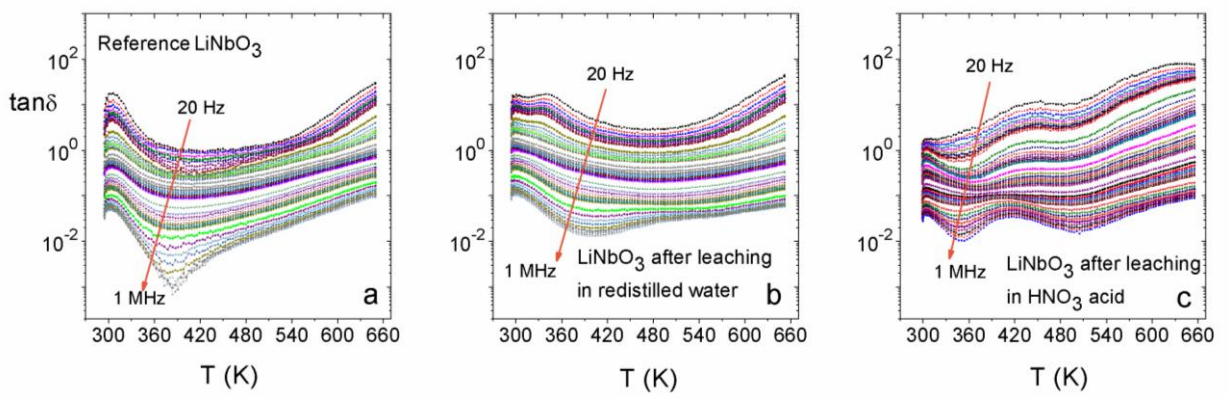

FIG. 28 The dielectric loss coefficient *tanδ vs.T* dependencies. Measurements conducted on crystalline powder samples of the $LiNbO_3$: (a) reference, (b) leached in the redistilled water, and (c) leached in the nitric acid.

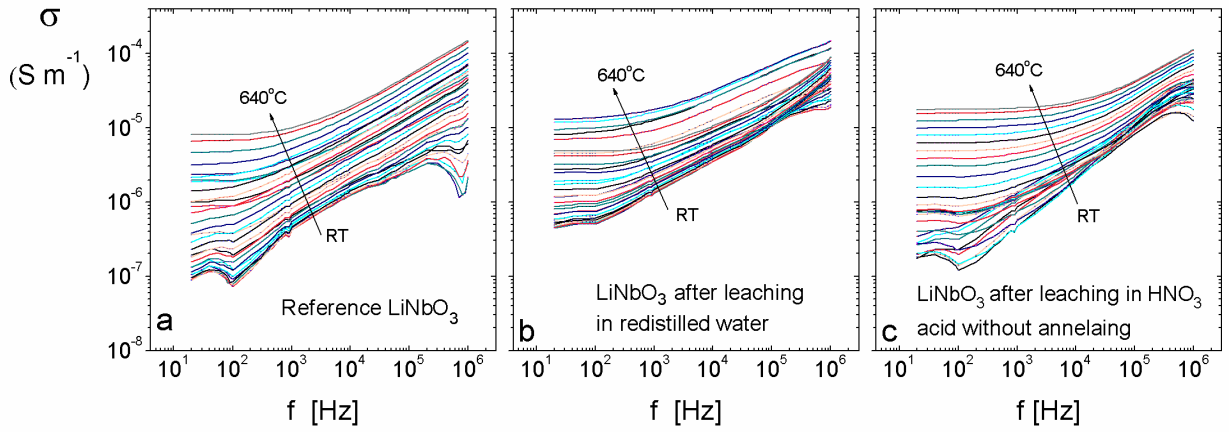

FIG. 29 The electric conductivity *σ vs. f* dependencies. Measurements conducted on crystalline powder samples of the $LiNbO_3$: (a) reference, (b) leached in the redistilled water, and (c) leached in the nitric acid.

The electric conductivity *σ vs. f* dependence was shown in Figure 29. These plots exhibited a frequency dependent electric conductivity, $\sigma \propto A f^{S}$, in a high temperature range. The saturation was reached at low range of frequencies [62]. This effect confirmed the dc conductivity contribution in the samples. The highest dc contribution was observed for sample leached in the nitric acid (see Figure 29(c)). For comparison, the Arrhenius plots of the electric conductivity vs. reciprocal temperature dependence, obtained at *f*=100 Hz (see Figure 30). The trend related to thermal activation of the conductivity occurred in the

T > 550 K range. On contrary, a positive temperature coefficient in resistivity (PTCR) was visible for lower temperature.

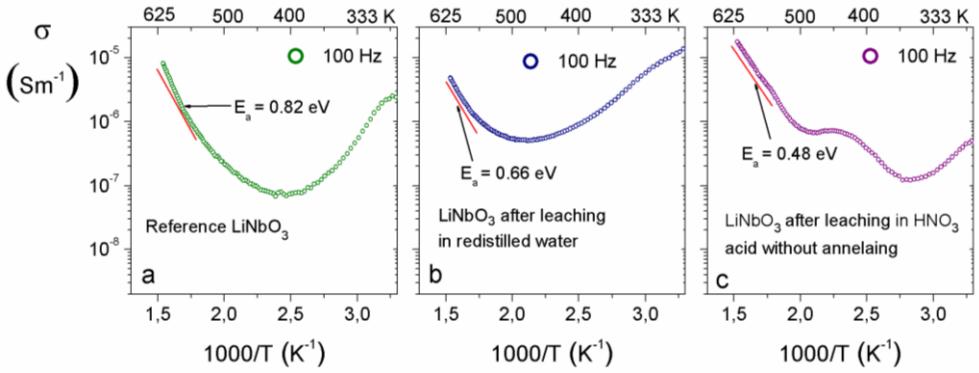

FIG. 30 The electric conductivity *σ vs.* reciprocal temperature T^{-1} dependencies measured at *f*=100 Hz. Measurements were carried out for crystalline powder of the $LiNbO_3$ samples: (a) reference and (b) leached in the redistilled water, and (c) leached in the nitric acid.

From dc resistivity data, showed in the Arrhenius plots of R_{dc} vs. T^{-1} (see Figure 31 and Figure 32), the activation energy E_a was estimated for each samples. The reference sample exhibited two activation energy values: E_a=1.11 eV in 550 to 630 K and E_a=0.83 eV [63] in 500 to 560 K ranges. The value E_a=1.11 eV corresponded to a behaviour of the space charge in the lithium niobate [64]. Moreover, the reference sample showed the highest value of the resistivity. Such E_a value was reported and assigned to oxygen vacancies.

The decrease in E_a value was observed for the leached samples. The lowest activation energy E_a=0.48 eV (see Figure 32(a)) occurred for sample leached in the nitric acid environment. After subsequent annealing processes, with upper limit: first at the 350 K (Figure 32(b)), second at the 650K (Figure 32(c)), the E_a increased. One can noticed that the E_a value changed after annealing and had a tendency to obtain on the similar value as the E_a estimated for the sample leached in the redistilled water (Figure 31(b)). To explained occurrence of this phenomenon in framework of the combined effect of the ionic migration. The migration of the hydrogen ions, which were previously embedded in the crystal lattice, due to the proton exchange reaction, was considered. Moreover, a simultaneous adsorption of the oxygen ions from the ambient air may have induced the observed change in the activation energy (compare Figure 31(b) and Figure 32(c)).

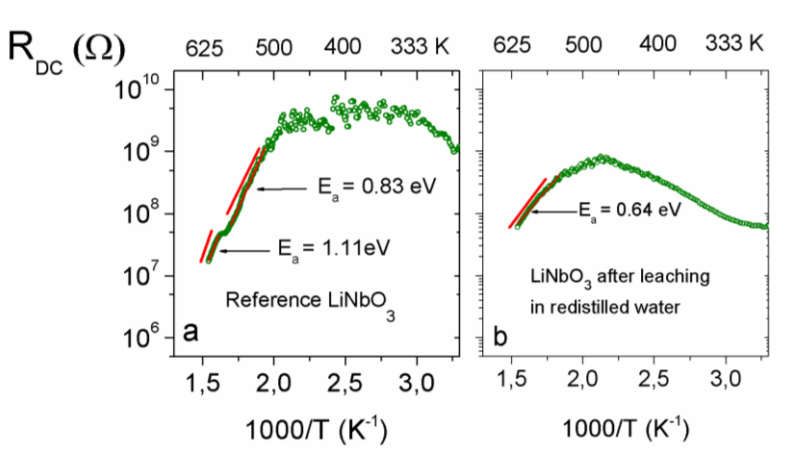

FIG. 31 The electric resistivity R_{dc} *vs.* reciprocal temperature T^{-1} dependencies. Measurements carried out in the crystalline powder samples of the $LiNbO_3$: (a) reference and (b) leached in the redistilled water.

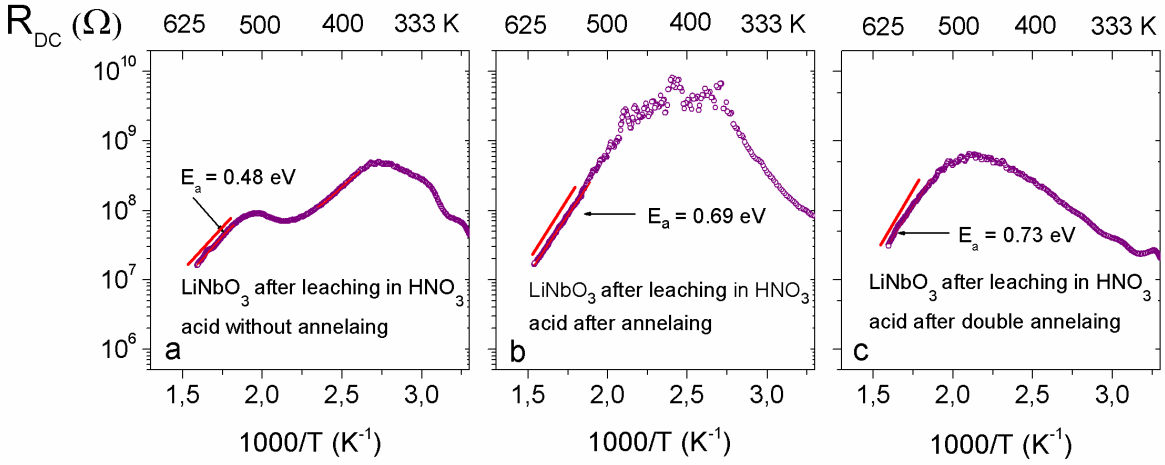

FIG. 32 The electric resistivity R_{dc} *vs.* reciprocal temperature T^{-1} dependencies. Measurements carried out in the crystalline powder samples of the $LiNbO_3$ leached in the concentrated nitric acid: (a) sample without annealing, (b) sample after annealing, and (c) sample after double annealing.

It is worth to notice, that the lithium niobate samples exhibited a positive temperature coefficient in resistivity (PTCR) effect, similarly to the other double oxide materials [65, 66]. We observed the PTCR for samples leached in the acid from the range of 300K to 370K (Figure 32(a) and (b)). For the sample leached in the redistilled water, for the sample leached in the nitric acid, and after double annealing (Figure 31(b) and 32(c)) the PTCR occurred in the temperature range from 300K to 500K. The occurrence of the PTCR effect was reported for the ferroelectric double oxides materials, which were electrically non-homogeneous. It was pointed that the oxygen vacancies and cations vacancies influenced significantly the

PTCR characteristics [67, 68]. The studied herein lithium niobate crystalline powdered samples were also non-homogeneous. It was determined with the use of the ICP-OES test that the leaching in water led to migration of the Li and the Nb ions to the solvent and consecutively the occurrence of the oxygen vacancies and cations vacancies in the surface of crystallites. Another type of surface non-homogeneity could be proposed for the samples leached in the nitrite acid. In this case, the conducted protonization led to replacement of the Li^+/H^+, that generated the $H_xLi_{1-x}NbO_3$ component of the surface.

3.1.5 Phase transition detection

Brillouin scattering spectroscopy provides useful information about elastic properties of the materials through the study of the sound velocity and attenuation which are related to the elastic constants and relaxation times of phonons. Therefore, this technique becomes a useful tool to obtain information on the defects within the crystal lattice. The study of the acoustic properties in nonstoichiometric samples is directly related to the applications of the optical and acoustic waveguides produced by proton exchanged lithium niobate where the effect of the lattice defects is similar [69].

The results obtained from the Brillouin spectroscopy were shown in Figure 34 and Figure 35. Data occurred for the transverse acoustic (TA) mode *vs.* Brillouin shift, exhibited a phase transition of the lithium niobate for pure and two protonized samples.

The Curie's temperature for all measured samples was similar. The value of the T_C was equal to 1120 °C, obtained result was lower than the literature reports by Volk and co-workers (T_C≈1140 °C). The differences in value of the T_C could be assigned to differences in the [Li]/[Nb] ratio, which resulted from congruency of lithium niobate. Lower value of the T_C corresponded to deficiency of the lithium ions in the crystal. The proton exchange reaction did not have influence on the T_C value. Detected melting temperature was equal to T_m≈1230 °C, sample after melting was shown in Figure 33.

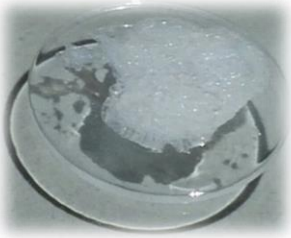

FIG. 33 Melted lithium niobate.

For data obtained for longitudinal acoustic (LA) mode *vs.* Brillouin shift (Figure 35), it was detected an additional anomaly at the temperature $T \approx 1050$ °C. This anomaly was observed only for protonized crystals. Bigger anomaly was noticed for sample with longer time of the protonization. It is worth to note, that Brillouin scattering is the volumetric measurement. Therefore, we deduced that the volume of protonized surface layer, related to the depths of the 380 nm (for protonization time t=480 h), was sufficient enough to produce the significant response (see Figure 35). The ratio of the volume of the pure crystal sample V_0 to the volume of the sample modified by proton exchange reaction V_{PE} was equal to V_{PE}/V_0=0.06% . This effect could be discerned also in TA mode as a bump in the vicinity of $T \approx 1050$ °C (see Figure 34).

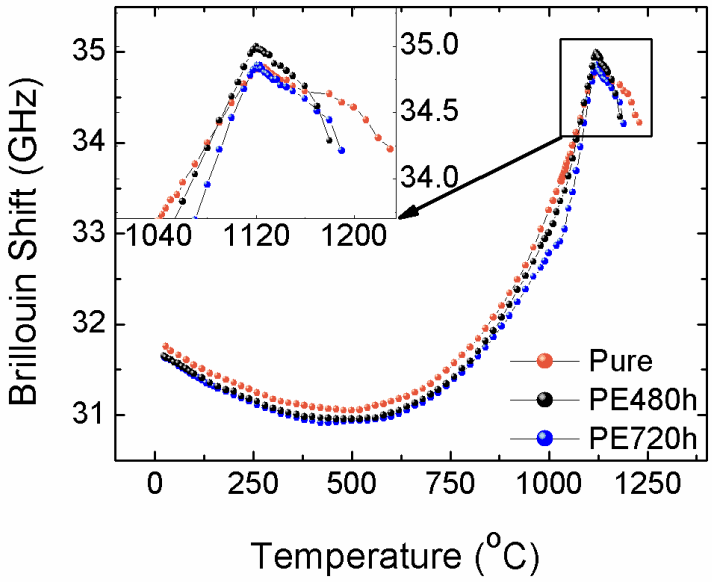

FIG. 34 Phase transition identification with use TA mode for pure, and two protonized samples, with protonization time 480 h and 720 h respectively.

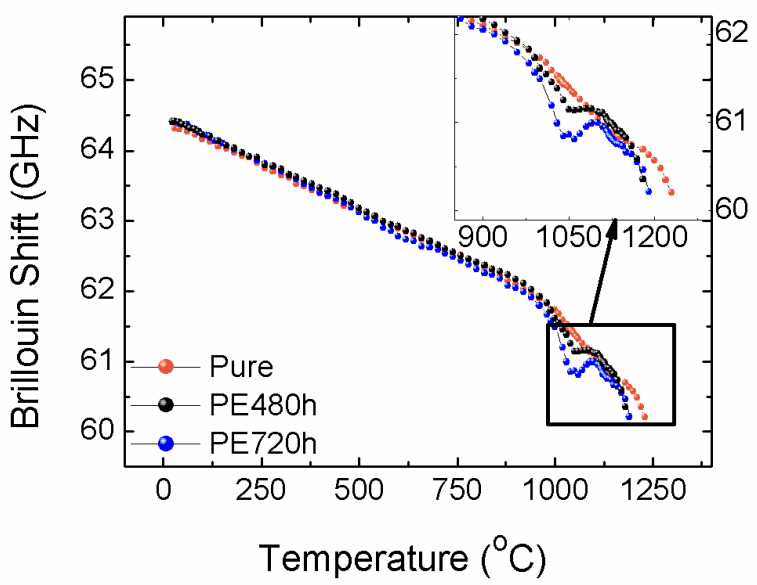

FIG. 35 LA mode vs. Brillouin shift distribution obtained for pure, and two protonized samples, with protonization time 480 h and 720 h respectively

3.2 Surface sensitive studies

Second aspect of my research was related to detailed analysis of the surface of the lithium niobate. The surface of pure crystal was measured with using several surface sensitive methods. The significant deficiency of the lithium ions in the surface of the *as-received* crystal, identified by the XPS measurement, was stimulating for additional measurements, which may explain this surprising result.

3.2.1 Surface composition of congruent $LiNbO_3$

The XPS test was conducted to define the atomic concentration of the elements of lithium niobate and to determine the changes in the spectra of each states during the high temperature treatment. The measurement was obtained on the epi-polished surface and on the cleaved $LiNbO_3$ crystal samples at the room temperature. The cleaved surface of the lithium niobate showed congruent ratio of the lithium to niobium elements. These results were assumed as the reference data for the studied as-received congruent crystal. Moreover, the test was performed also on the *as-received* epi-polished surface layer. Such outer epi-polished surface had shown markedly low concentration of Li ions, which did not exceed 4 at% (see Table 3). It is worth noting that similar low ratio [Li]/[Nb]=0.3 was reported by Tabata *et al.* [40] for as-received surface layer of the lithium niobate crystals.

TABLE 3 The atomic concentration estimated from Li 1s, Nb 3d, and O 1s lines intensity. The XPS spectra were obtained for the as-received cleaved and epi-polished $LiNbO_3$ samples, measured at room temperature.

as-received crystal	Li 1s	Nb 3d	O 1s	[Li]/[Nb]
cleaved	17 %	25.5 %	57.5 %	0.67
epi-polish surface	1 %	25.7 %	73.3 %	0.04

The XPS measurement was performed also on the epi-polished congruent crystal sample in the range of temperature from 300 to 900 °C and the survey spectrum in the energy range of 0–1400 eV was recorded. Carbon C 1s state (~284.5 eV) line occurred in the spectrum

obtained in the 300–500 °C range and it was assigned to contamination with carbon compounds (Fig. 36).

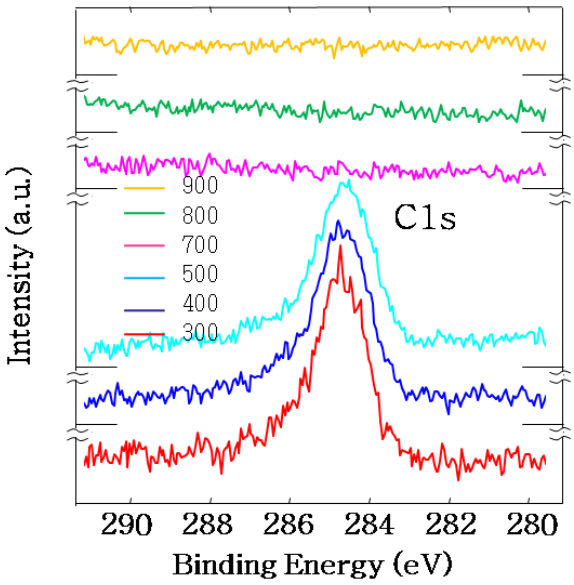

FIG. 36 The carbon C 1s core line. Spectrum measured at temperatures from 300 to 900 °C. The "zero" level in the intensity scale is shifted.

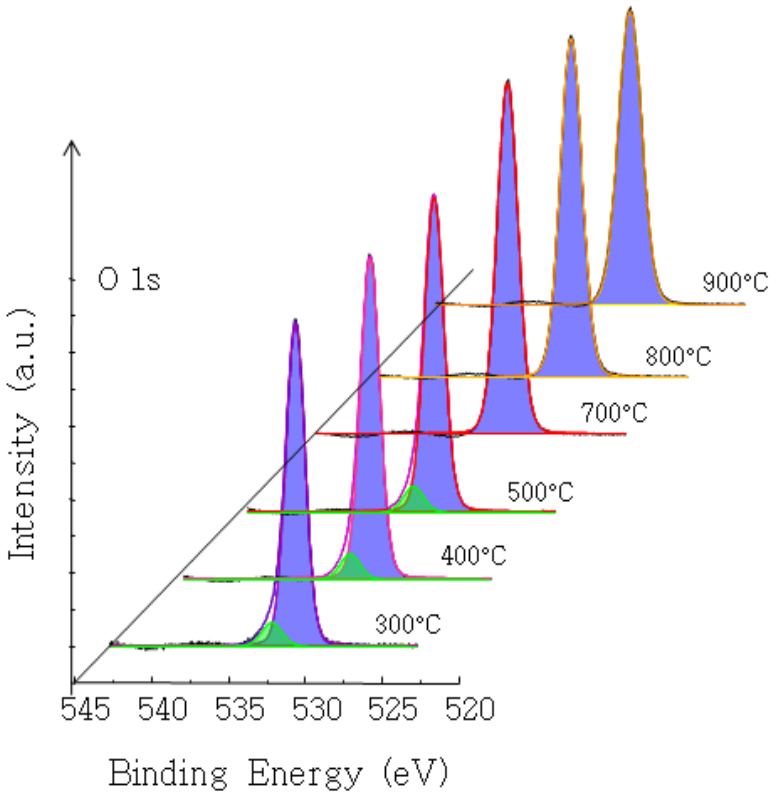

FIG. 37 The oxygen O 1s core line. Spectrum measured at temperatures from 300 to 900 °C.

The oxygen O 1s line, with the binding energy equalised to 530.5 eV, was shown in Figure 37. Numerical deconvolution exhibited two lines for the temperature range 300–500 °C. The minor intensity contribution was distinguished at higher binding energy (~532.5 eV). The occurrence of this minor O 1s core line corresponded to C 1s line and could be assigned to contamination with CO_2 compound because of the higher temperature range (annealing), the carbon compound contamination vanished.

The numerical fit showed that the Nb 3d core line consists of overlapping contributions (Figure 38). The Nb 3d core line, which was measured at 300, 400, and 500 °C, was split to three compounds (doublets). One Nb^{5+} $3d_{5/2}$ (207.5 eV) and Nb^{5+} $3d_{3/2}$ (210.2 eV) doublet (D1) was assigned to Nb ions placed in $LiNbO_3$ matrix. Therefore, was assigned to Nb ions placed inside the sub–lattice consisting of proper NbO_6 octahedra. For the second doublet (D2) contribution was observed at lower binding energy. It was proposed to assign to NbO_2 precipitation and/or cluster of defects (see Eq (2)). The doublet (D2), assigned to the states Nb^{4+} $3d_{5/2}$ (206.7 eV) and Nb^{4+} $3d_{3/2}$ (209.4 eV), might have corresponded to niobium ions at antisites, $Nb_{Li}^{4\bullet}$, and lithium vacancies, $V_{Li}^{'}$, which formed clusters of defects during the crystal's growth. The third doublet (D3) occurred at a still lower binding energy. It was proposed to assign the (D3) doublet to the Nb^{2+} $3d_{5/2}$ (205.6 eV) and Nb^{2+} $3d_{3/2}$ (208.3 eV) states of the niobium ions, *i.e.* it would originate from NbO oxide [70]. Such identification of the niobium charge states were supported by results reported for Nb-O thin films. Nowak *et al*. [13] showed that the occurrence of the Nb^{5+}, Nb^{4+}, and Nb^{2+} states depended on temperature of the reduction conducted at the UHV condition.

On the contrary, the Nb 3d line, measured at 700, 800, and 900 °C, showed only one doublet (D1), typical for oxidation state of niobium Nb^{5+} $3d_{5/2}$ and Nb^{5+} $3d_{3/2}$. This main contribution, related to niobium ions Nb^{5+} state, was observed in all temperatures.

The Nb 4s state line (see Figure 39), placed at 60.7 eV (compare paper by Steiner *et al.* [71]) occurred at each temperature from the 300–900 °C range. On contrary, the Li 1s core line (55.4 eV) [72, 73, 74, 75], which occurred in vicinity of 56 eV, was detected only when the spectrum was measured at 700, 800, and 900 °C. Hence, the identification of the Li 1s line was univocal. Moreover, such result was consistent with the XPS measurement conducted at the room temperature (see Table 3, Table 4, and Figure 39).

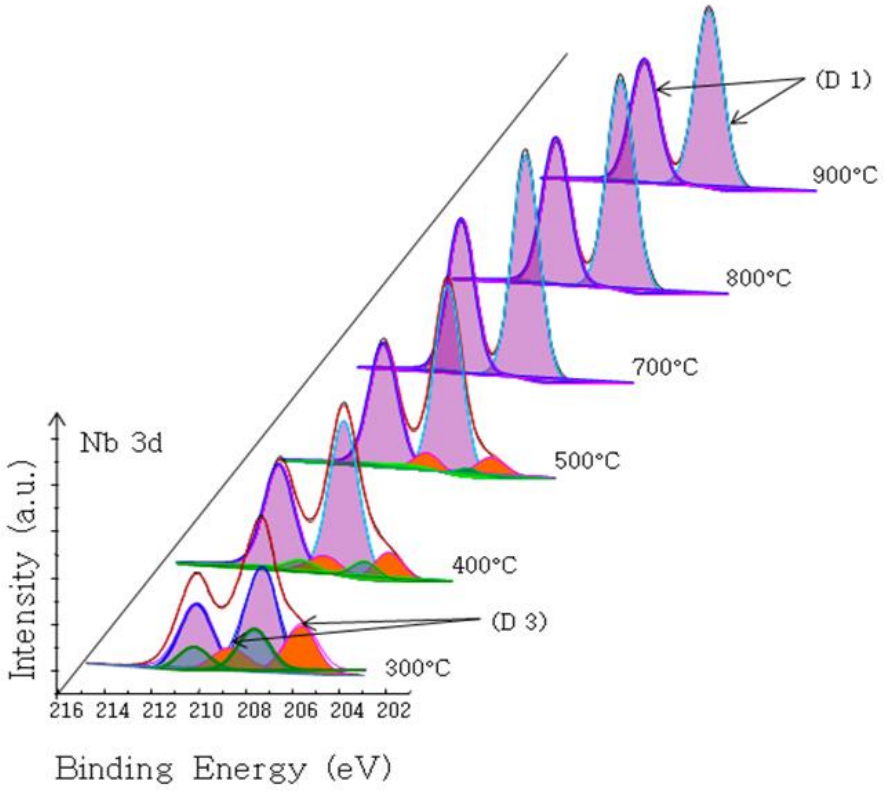

FIG. 38 The niobium Nb 3d core line measured at temperatures from 300 to 900 °C. The split in to three doublets was performed for spectrum obtained at 300, 400, and 500 °C. Colour code: doublet (D1)–violet; doublet (D2)–green; doublet (D3)–orange.

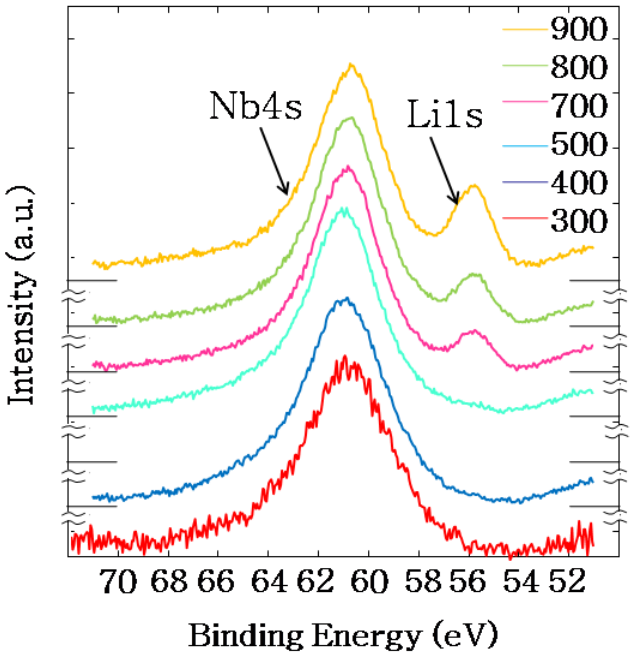

FIG. 39 The niobium Nb 4s and lithium Li 1s spectrum. The "zero" level in the intensity scale is shifted.

Atomic concentration of the lithium and niobium were shown in Table 4. Such a non-typical result correlates to the results of TOF-SIMS test, presented below. A similar effect was reported by Tabata *et al.* [40] that the deficiency of Li ions occurred in surface layer, which is in contrary to proper composition of the bulk. Differences between the resulted obtained for atomic concentration analysis, in terms of the literature data [Li]/[Nb]=0.94, may indicate the existence of an easy diffusion paths. Therefore, the improvement of the chemical composition of the surface layer could be achieved by thermal treatment conducted in the high temperature range (see Table 4).

TABLE 4 Atomic concentration of lithium and niobium derived from XPS spectra of the Li 1s and Nb 3d lines obtained for as-received epi-polished $LiNbO_3$ sample.

T (°C)	Li	Nb	[Li]/[Nb]
300	0	100	0
400	0	100	0
500	0	100	0
700	14.46	85.54	0.17
800	19.58	80.42	0.24
900	34	66	0.52

The lithium niobate valence band (VB) consisted of the oxygen O 2p states hybridized with niobium Nb^{5+} 4d states [15, 76] (Figure 40). The valence band was extended to the ~3.5–10 eV range. However, at lower temperatures (300–500 °C), there was an additional line which was visible in vicinity of Fermi energy (Figure 40). In accordance to literature XPS and UPS measurements [13, 77, 78] such a line could be related to surface defects. Hence, it was proposed to assign to the Nb 4d states.

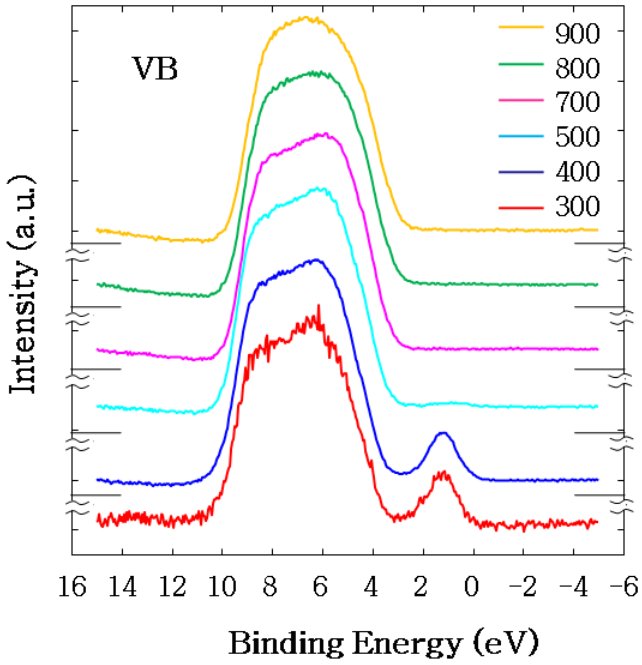

FIG. 40 The valence band region of the spectrum. The "zero" level in the Intensity scale is shifted.

It is worth to point out that the Nb^{4+} 3d states, the Nb^{2+} 3d, the minor contribution to O 1s, and also the carbon C 1s states were detected only at the 300, 400, and 500 °C. Hence, the XPS test discerned two temperature ranges, related to the surface layer features. The spectra, which were obtained in the 300–500 °C range showed additional charge states. They could be assigned to the point defects and clusters of defects which were well known in the literature [14, 15, 16, 78].

3.2.2 Leaching and lithium deficiency

The lithium ions deficiency detected from the XPS test, was explained in accordance to the preparation of the epi-polished surface of the samples since this procedure had been performed in water solutions. Therefore, the actual concentration of the lithium ions in the surface layer was analysed with the use of the leaching procedure. After leaching the blank probe and the samples, were measured alternately four times (for blank probe and crystal sample with rough surface) or three times (for crystal sample with epi–polished surface), with three individual exposures per measurement. For crystal sample with rough surface, the emission lines Li 670.7 nm (both in axial and radial view), Li 610.3 nm, and Nb 313.0, 316.3, 319.4 nm (all axial) were evaluated. Due to the very low concentration in the leaching solution of crystal sample with epi–polished surface, only the emission lines Li 670.7 nm

and Nb 309.4 nm (both axial), which had the lowest limit of detection, were considered for evaluation.

No Li and Nb ions could be detected in the blank reaction. The main value of the evaluated emission lines and the weight of the solution were used to calculate the total content of the elements leached into the water. A total of 0.95 ± 0.08 μmol = 6.57 ± 0.50 μg of Li and 0.194 ± 0.007 μmol = 18.02±0.67 μg of Nb was found in the leaching solution for crystal sample with rough surface, whereas only 5.83 ± 0.19 nmol = 40.44 ± 1.29 ng of Li and no Nb ions (<0.14 nmol = 12.9 ng, the detection limit) were detected in the leaching solution for the crystal sample with epi–polished surface. The lithium niobate reaction with dissociated water could proceed as follows:

$$\begin{aligned} &LiNbO_3 + xH^+ + xOH^- + (1-x)H_2O \longrightarrow \\ &Li_{1-x}NbO_3 + xLi^+ + xOH^- + (x/2)H_2 \uparrow + (1-x)H_2O \end{aligned} \qquad (12)$$

Hence, the lack of the Li ions in the surface layer, as measured by the XPS in the 300–500 ^{o}C range, could be assigned to preparation stage, since the epi-polishing was carried out with the use of the water solution. On the contrary, the occurrence of the Li line at the higher temperatures resulted from another effect. The migration of the Li ions from bulk toward surface occurred, and was verified with the use of the TGA, effusion, and TOF-SIMS tests.

3.2.3 Mass changes during reduction and oxidation process

The analysis of the TGA results was conducted to determine the quantity of the mass changes in the $LiNbO_3$ samples. The leaching procedure exhibited a deficiency of the lithium ions in the surface layer. Therefore, there were prepared four samples: *as-received* epi-polished crystal *as-received* crystal with rough, scraped surface and two powdered crystalline samples. Epi-polished samples showed different roughness of surface, measured with the use of the atomic force microscopy, on the 3x3 mm^2 area, *i.e.*, the values of RMS=0.19 nm and RMS=0.38 nm were obtained, respectively. Figure 41 exhibited particles diameter distribution determined for the two powders used for the TGA tests. The powder particles showed the average diameter value of the ~85 μm and maximum at ~110 μm, while the particles were distributed within the ~0.2–300 μm range. The fine powder particles had the average diameter value of the ~25 μm and maximum at ~40 μm, while they exhibited the occurrence of two fractions, which were distributed in two ranges, ~0.05–2 μm and ~2–120

μm, respectively. The other two powdered samples with various grain size distribution were also prepared. The purpose was to verify whether the samples with different ratio of the surface layer volume to the bulk volume showed various efficiencies, which might correspond to the decomposition process.

The reduction procedure results were shown in Figure 42. The plot exhibited changes of the normalized quantity of the mass of samples, with respect to the starting mass in each subsequent step of thermal treatment. Measurement conducted at 500 °C did not show any change in the mass of the sample. The mass loss had been detected after reduction treatment conducted at the higher temperatures. Therefore, reduction process started from the 600 °C effectively for each type of the samples. The relative sample mass changes *vs.* time, were normalized for each step. The marked similar changes in the mass of the crystal sample due to thermal treatment, occurred both at the temperature of 900 °C and 1000 °C in case of the as-received crystal with epi-polished surface (Figure 42(a)). In case of the as-received crystal with rough surface, the major mass loss had occurred for the last stage of annealing, conducted at 1000 °C (Figure 42(b)). In case of the powder (Figure 42(c)) and fine powder (Figure 42(d)), the major mass losses had occurred for the last stage of the annealing conducted at the 1000 °C, while moderated changes occurred for the annealing at the lower temperatures. Therefore, one could deduce that the loss of mass depended on the surface volume to bulk volume ratio.

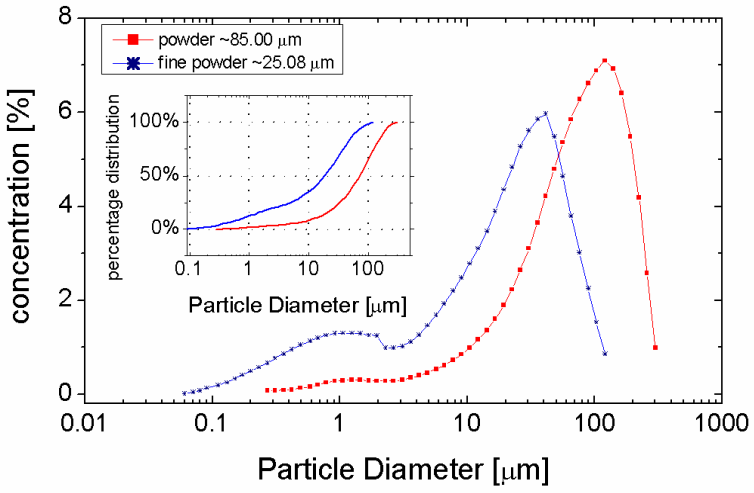

FIG. 41 Particle diameter distribution for two powders used in thermogravimetric test.

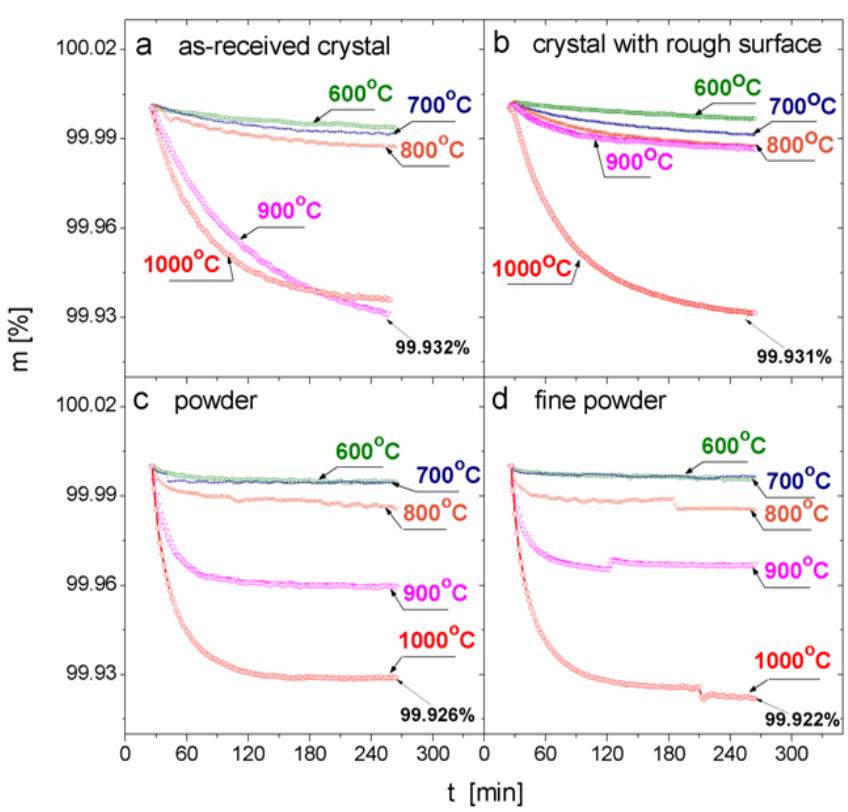

FIG. 42 Thermogravimetry analysis conducted on as-received epi-polished crystal (a), as-received crystal with rough surface (b), powder (c), and fine powder (d). The samples were annealed in reduction conditions of 96% Ar + 4% H_2 mixture, in the range of temperatures of 600–1000 °C.

The total loss of the mass corresponded to the relative loss of ~0.15%. Such a high quantity indicated the marked reactivity of the $LiNbO_3$ sample with the hydrogen gas flowing at high temperature. Studies of decomposition with the use of the TGA tests showed that reduction conditions were efficient in the temperature higher than 800 °C for the powders and in the temperature higher than 900 °C for the crystals. For crystal samples, this migration-related process was not saturated even for ~4 hours. In case of powders (Figures 42 (c) and (d)), saturation occurred after a certain time, within 2 hours, when the migration of ions followed by their evaporation was fulfilled. It was noticed that a more efficient loss of mass, at lower temperatures, occurred for the particles with higher ratio of surface layer volume to bulk volume.

The measurement conducted in the mixture of 79% Ar +21% O_2 corresponded to the expected oxidation process. The mass m_0=35.80 mg of the oxidized sample did not change ($\Delta m \approx$+/- 0.02%). It was deduced that oxygen did not build to the sample at applied oxidation conditions (see Figure 43).

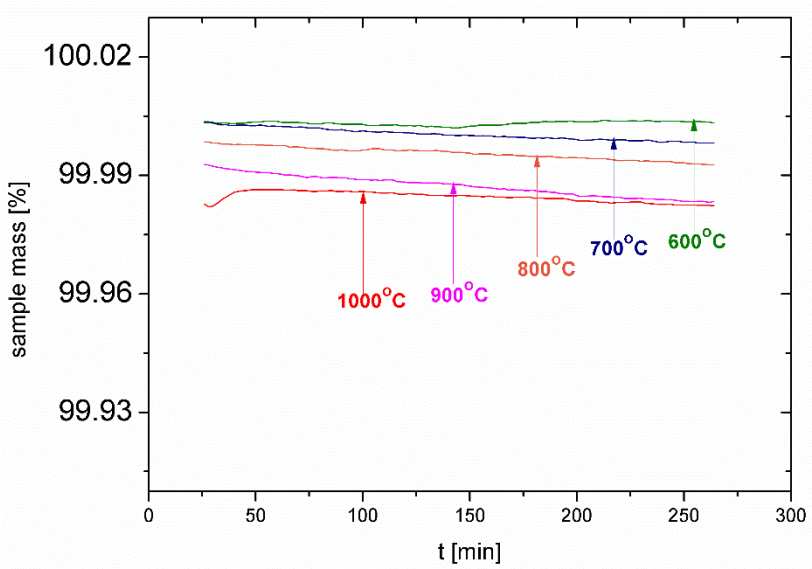

FIG. 43 Thermogravimetry analysis conducted on as-received epi-polished crystal. The samples were annealed in oxidation conditions of 79% Ar +21% O_2 mixture, in the range of temperatures of 600–1000 °C.

The TGA test showed that the oxygen content could not have been increased within the experimental accuracy. Therefore, the congruent $LiNbO_3$ crystals were stable with respect to the provided oxidising conditions. On the contrary, the reducing conditions decreased the mass of the tested samples. In the experiment, the loss of mass for all samples was markedly higher at temperatures of the 900 and 1000 °C (see Figure 42). Another important effect was related to the gradation size of the powder particles and crystals. It occurred that smaller diameters of the particles enabled more efficient mass loss at the lower temperature of 800 °C. It was expected that long-term experiments conducted at a temperature higher than 1000 °C and for time longer than several hours would lead to decomposition of the samples (the melting point occurred at ~1200 °C). A similar effect had been reported for $NaNbO_3$ crystals [79], since it was determined that the decomposition of those crystals might occur at $T \geq 800$ °C under reducing conditions. Therefore, the effusion test on $LiNbO_3$ crystals was carried out at lower temperatures of T=800 and 900 °C.

3.2.4 Identification of released species

Effusion processes were conducted at two temperatures the 800 and 900 °C, under UHV conditions. Data analysis allowed to identify which compounds had been released from $LiNbO_3$ surface. Figure 44 showed the partial pressure of the components released from surface of the samples at the chosen temperatures.

Figure 44(a) matched the two most volatile compounds, *i.e.* lithium oxide, Li_2O, and atomic oxygen, O. The determined pressures were of the order of $5 \cdot 10^{-8}$ bar for atomic oxygen O at 900 °C and $1.5 \cdot 10^{-8}$ bar for atomic oxygen O at 800 °C. For the Li_2O molecule the pressure values were: $1.4 \cdot 10^{-8}$ bar at 900 °C and $2.6 \cdot 10^{-9}$ bar at 800 °C, respectively. The molecular oxygen O_2 also showed slightly lower pressure temperature dependence, of the order of 10^{-10} bar (Figure 44(b)). It is worth noting that after ~1 h, the effusion rate of these species changed and partial pressures dropped to $\sim 3.3 \cdot 10^{-9}$ bar for atomic oxygen and to $\sim 2.8 \cdot 10^{-10}$ bar for Li_2O. Moreover, the partial pressures of the Li, LiO, and NbO were lower for about two (at 800 °C) and three (at 900 °C) orders of magnitude than the Li_2O partial pressure at both temperatures, respectively (Figures 45(a) and (b)). Hence, the effusion yield of the released products converged to the low values of partial pressure: $\sim (1–4) \cdot 10^{-11}$ bar after the drop (Figure 45, inset). One could deduce that crystals reached a thermodynamically more stable or less efficient state, which occurred after ~60–70 min.

The effusion test proved that atomic oxygen, O, lithium oxide, Li_2O, and molecular oxygen, O_2, were the main species which were released from the $LiNbO_3$ crystal samples (Figure 44). Moreover, the other species, Li, LiO, and NbO, were also detected and the partial pressure value, which was about two orders of magnitude lower in this case (Figures 44 and 45). Therefore, the O and Li ions were able to migrate from the bulk towards the crystal surface to the topmost surface layer. Then they released and reacted immediately with each other in the vicinity of the surface. An anomaly in the partial pressure was detected, *i.e.* a drop in plots occurred after ~60–70 min of measurement (Figures 44 and 45). For instance, the partial pressure of atomic oxygen O and of Li_2O dropped. The values, which were estimated after the drop, were closer to the values measured for the Li and LiO.

Out-diffusion kinetics were considered for the $LiNbO_3$ crystals [80]. From the measurement of partial pressure of the flux over the $LiNbO_3$, the mass loss had to be assigned both to the Li_2O and to oxygen diffusion, followed by the desorption of the molecules from the crystal surface. It is worthwhile to note that there was identified a variety of lithium and oxygen species, *i.e.* Li, LiO, Li_2O, O, and O_2 released from the $LiNbO_3$.

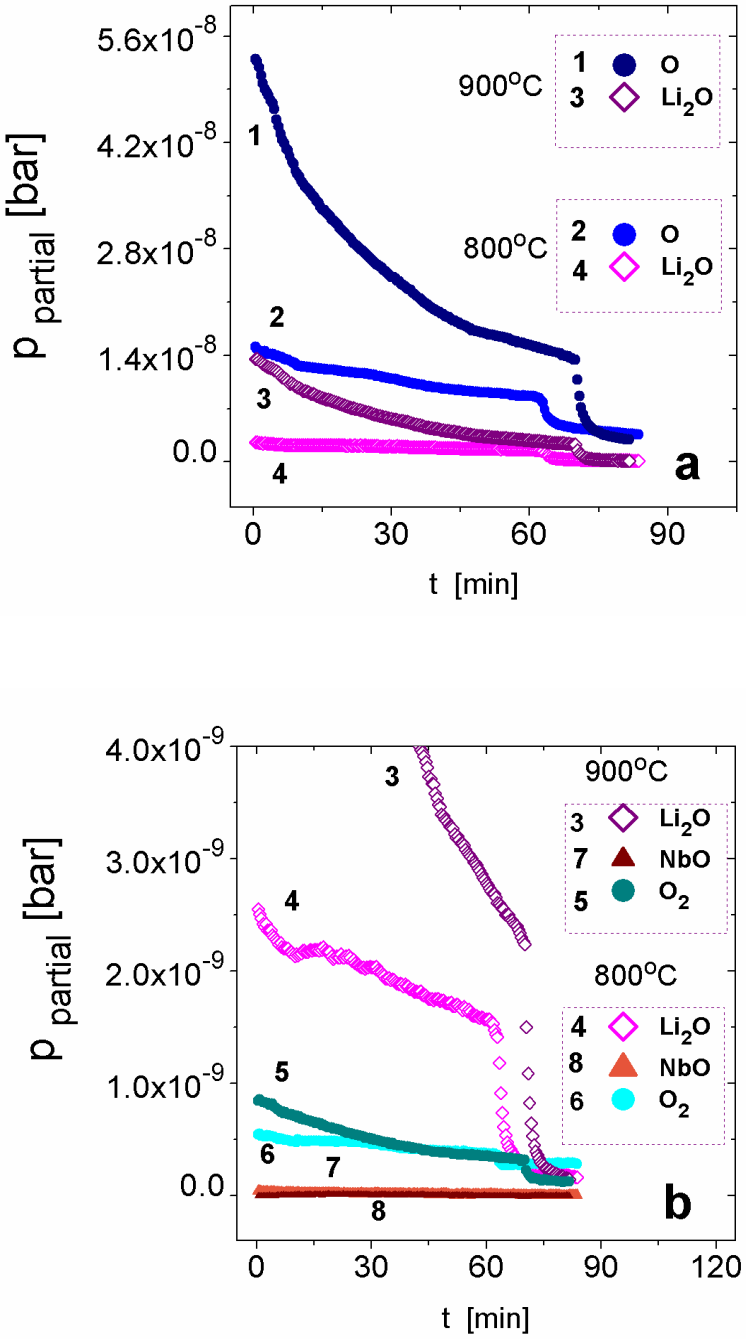

FIG. 44 Comparison of partial pressure *vs*. time dependence of released components detected for two effusion processes conducted at 800 and at 900 °C. (a) The graph shows the comparison of effusion test results for two dominating species, O and Li_2O. (b) The partial pressure of less efficient species.

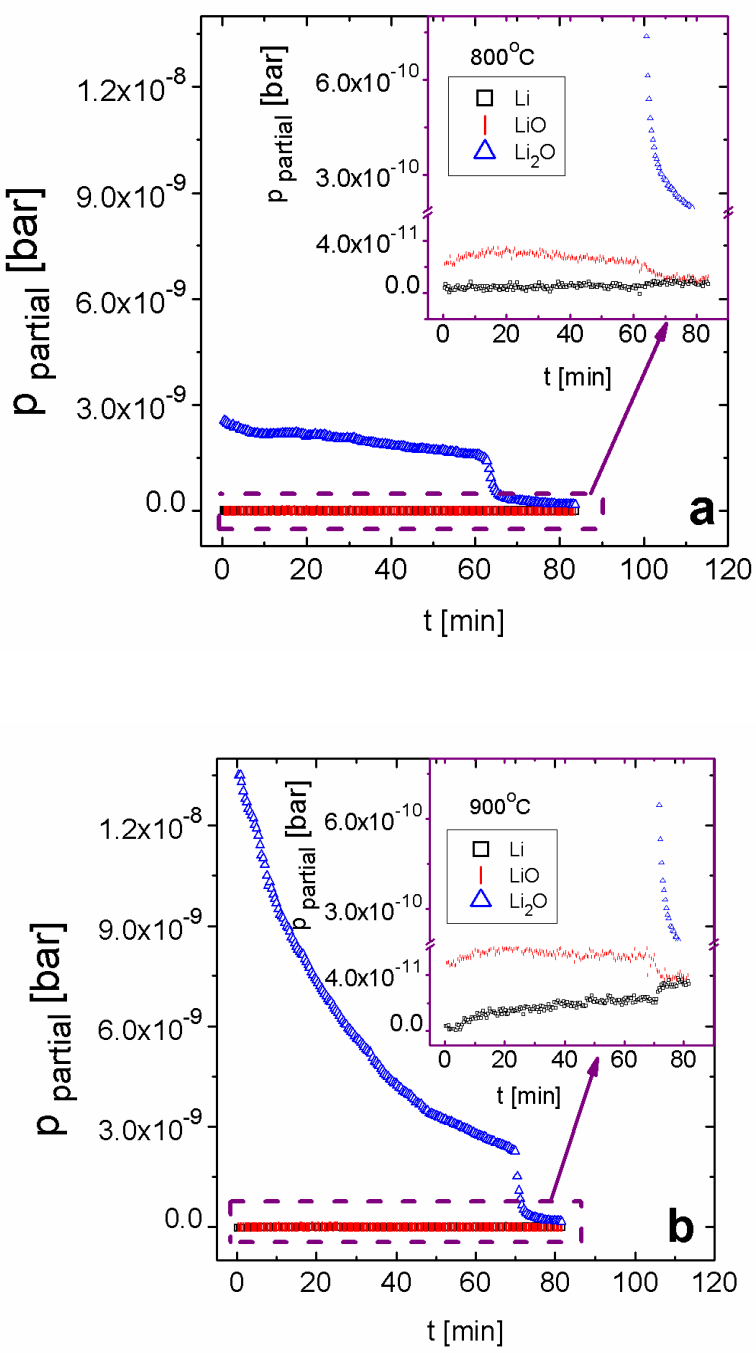

FIG. 45 The partial pressure of the released lithium components: Li, LiO, and Li_2O, measured for effusion process conducted at two temperatures: 800 °C (a) and 900 °C (b). Inserts show Li and LiO partial pressure dependences, which correspond to much less-efficient processes.

3.2.5 Non – homogenous distribution of ions

TOF-SIMS tests were conducted to check the influence of the reduction process on the $LiNbO_3$ chemical composition in the surface layer. Spatial distribution of the selected elements was analysed. For obtained results the matrix effect was hardly avoided. In case of the ABO_3 double oxides, the ionic complexes were more efficiently removed from the AO sublattice, than from the BO_2 sublattice. Indeed, we observed the enhanced number of counts related to the Li-O complexes, both from the reference and the reduced lithium niobate samples. Therefore, it was referred the ratio of the Li and Nb concentration, *i.e.*, [Li]/[Nb] quantity, and not to the absolute values.

The data obtained from the SIMS measurement (showed in Figure 46) were recalculated with the use of the double normalization procedure. First normalization showed specific depth profile for three different reduction temperatures. Second normalization led to the [Li]/[Nb]≈1 values for deeper part of the crystal, which showed homogeneity of the interior of the studied crystals. As a result of this calculation we received three curves with comparable scale.

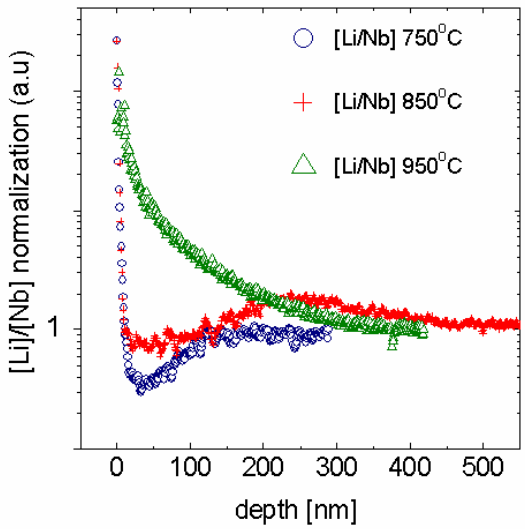

FIG. 46 Depth profile of the normalized [Li]/[Nb] distribution ratio, which resulted from diffusion of the ions towards the surface.

The measurements conducted on samples, which were reduced *ex situ* at 750 and 850 °C, showed similar effects (Figure 46). The outermost layer (0–20 nm) exhibited an increased content of the Li ions. The intermediate part of the surface layer (~20–200 nm) showed decreased values of the [Li]/[Nb] ratio that corresponded to deficiency of the Li ions.

One could see that saturation at the [Li]/[Nb]≈0.94 ratio, expected for congruent crystals, occurred starting from ~240 nm for *T*=750 °C and from ~500 nm for 850 °C, that corresponded to the congruent features which were stable in the deeper parts of the surface layer. It was deduced that this variation in depth profile could be attributed to the effect of non-uniform migration of the Li and Nb ions, respectively. The segregation of the Li and Nb ions, which was detected within the surface layer, resulted from the diffusion of the Li ions from the bulk or from the deeper part of the surface layer, towards the surface, and finally outside the crystal. On the contrary, the [Li]/[Nb] ratio decreased steadily over the whole depth range, when measurement proceeded on the sample reduced at the 950 °C. Such non-saturated depth profile suggested a different mechanism of diffusion. Moreover, such result might suggest that the Li ions were more volatile than Nb ions in these experimental conditions. Hence, the spatial distribution of Li ions was checked.

Characterization of the surface before and after sputtering was performed (see Figures 48 and 49). Sample before sputtering (Figure 48) showed very low concentration of the lithium and niobium in the surface. The crystal outward layer was covered by carbon compounds (see Figure 47). The carbon distribution was almost homogeneous for the sample. Carbon might originate both from crystal growth technology and from *ex–situ* contamination, *e.g.*, carbon dioxide. Similar result was observed in the XPS spectra which showed additional contribution of the carbon state in the temperature range from 300 to 500 °C (compare Figure 36). After sputtering (Figure 49) the surface of the crystal sample exhibited clear distribution of the lithium, niobium and oxygen compounds. The contamination layer was removed. Obtained data showed areas of higher concentration of the lithium ions. Those areas correlated with oxygen maps. One could deduce that observed lithium was in the of oxide form, which correlated with the model (eq. 8, p.17) describing migration of the lithium oxide compounds.

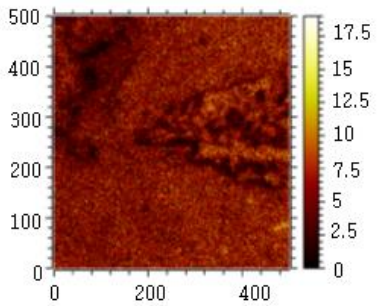

FIG. 47 TOF-SIMS maps, obtained before sputtering for the carbon contamination for sample reduced in 500 mbar atmosphere of deuterium for 2 hours at 950 °C.

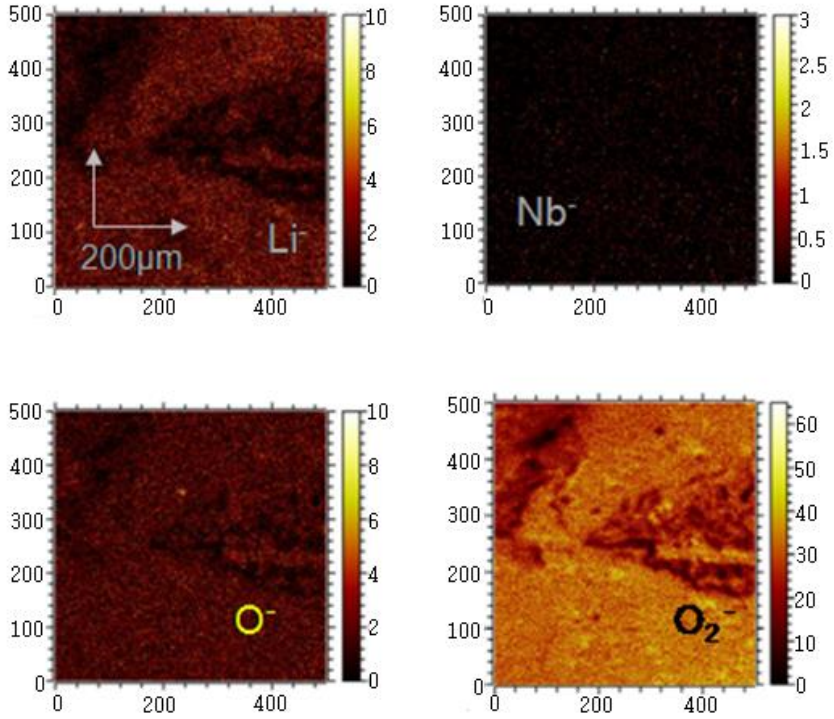

FIG. 48 TOF-SIMS maps, obtained for the lithium niobate crystals reduced in 500 mbar atmosphere of deuterium for 2 hours at 950 °C before sputtering.

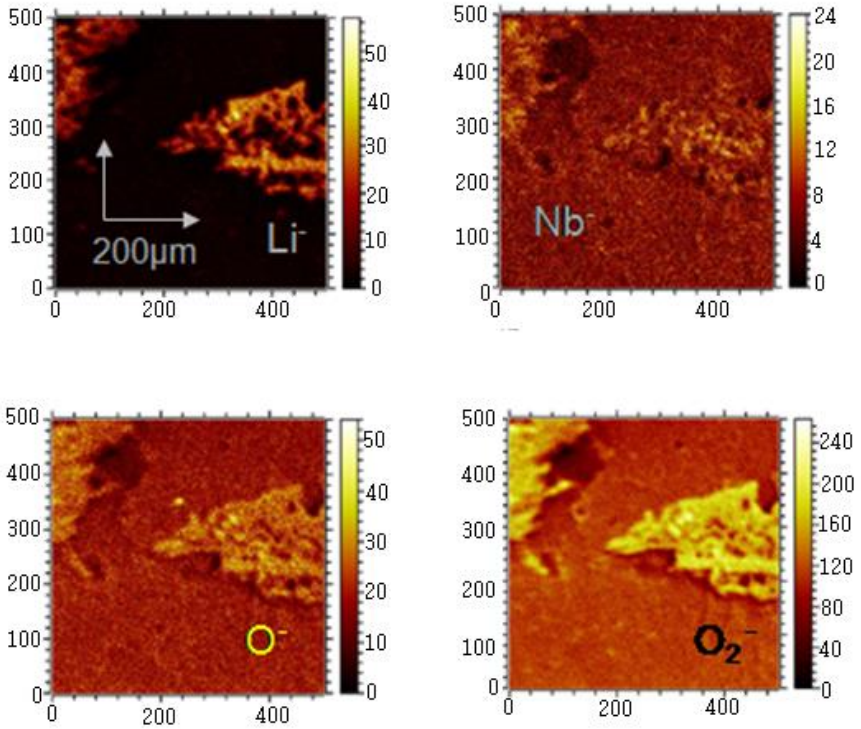

FIG. 49 TOF-SIMS maps, obtained for the lithium niobate crystals reduced in 500 mbar atmosphere of deuterium for 2 hours at 950 °C after sputtering.

The surface layer, on the image which was presented in Figure 50, exhibited a non-homogeneous distribution of the lithium and niobium in the matrix. The dark area in Li image was related to the Li deficiency in the deeper part of the surface layer. The [Li]/[Nb] distribution, obtained from the imposed Li and Nb images, revealed additional details. The triangular area showed non-homogeneity, which manifested as granular structure. The Li-rich areas (light blue colour) contained inclusions of the Nb-rich grains (red spots). A similar structure could be discerned in the upper left corner of the image. Moreover, there was a dark area in between, which corresponded to the Li-deficiency in the matrix.

Therefore, such non–homogeneity was consistent with the [Li]/[Nb] profiles (compare Figures 46 and 50). It would be noticed that the *as-grown* and epi-polished, *i.e.*, non-reduced samples exhibited uniform distribution of the elements. It was deduced from the TOF-SIMS profiles published in our former work [53].

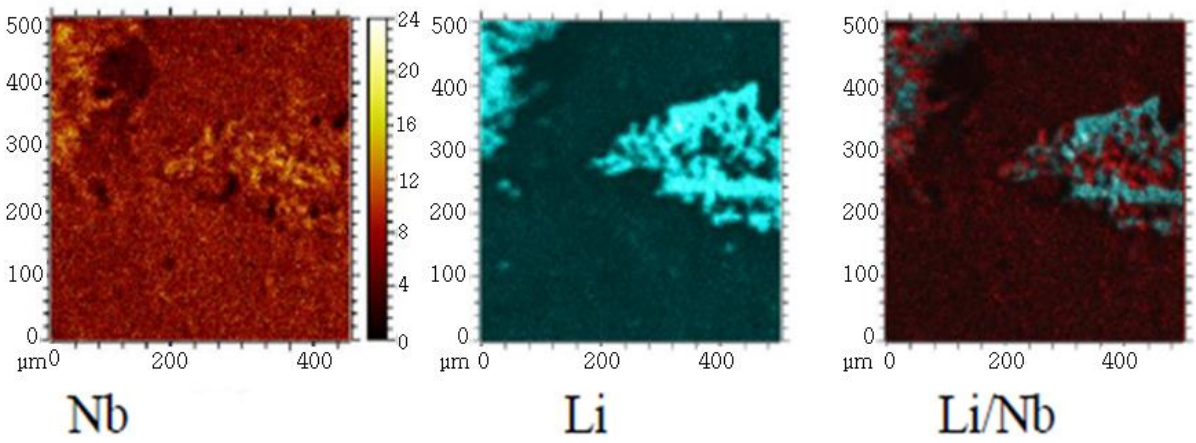

FIG. 50 Correlative TOF-SIMS maps, obtained for the sputtered lithium niobate crystals reduced in 500 mbar atmosphere of deuterium for 2 hours at 950 °C. From left to right: Nb anion distribution; Li distribution transformed to blue colour palette; the [Li]/[Nb], which has been obtained from the imposed Li and Nb maps.

It is worth noting that samples for the TOF-SIMS analysis were reduced with the use of the deuterium atmosphere. However, deuterium elements were not detected in the depths profile, hence they did not build into the lithium niobate crystal lattice. On the contrary, it showed in our former study that hydrogen ions had been built in to the crystal lattice when the samples were protonized with acid (HNO_3) [53].

4 Summary

In my study I was focused on the protonization process and ions segregation in the surface layer of the lithium niobate. The proton exchange reaction was confirmed with using several techniques. It occurred that the chemical composition of the actual surface of studied material was far from the composition of the bulk. I studied the conditions, which modifi a surface of the $LiNbO_3$, and I tried to determine conditions which could change composition in the surface.

Protonization of the lithium niobate crystals was started with creation and construction of a setup, which enabled conducting long term chemical reaction at the safe conditions. Properly prepared $LiNbO_3$, in the form of crystal and powdered crystalline samples, were measured. Methods used in the experiment verified the effectiveness of the proton exchange reaction.

The TOF-SIMS depth profile showed substitution of the lithium ions by the hydrogen ions (see Figure 23). It is worth to note that the PE reaction was not a linear process. The depth of protonization was not directly proportional in terms of protonization time, *i.e.*, for the PE time equal to 240 h the level of the ion exchange was equal to 250 nm and for 480 h the level was equal to 380 nm.

From the ICP-OES analysis it was estimated that the lithium concentration in the concentrated nitric acid solvent was about two orders of magnitude higher than the concentration obtained from the redistilled water solvent. Hence, leaching in the nitric acid, removed lithium from the crystal lattice much more effectively. This result could be explained by the ions replacement, since H^+, substituted Li^+ ions, which provided charge compensation in the $H_xLi_{1-x}NbO_3$ compound and blocked outward migrations of the niobium ions.

The XRD pattern analysis showed that the concentrated nitric acid induced structural transformation. The lithium niobate modified by the PE, with partially substituted Li^+ by the H^+ showed monoclinic symmetry (see Figure 26). Compounds, which appeared after the PE procedure, could have been assigned to niobium oxides precipitation and related to the niobium sublattice, where were visible as an additional lines in the pattern. The leaching reaction conducted at the redistilled water did not change the structure of the lithium niobate. Lower intensity of the reflections was assigned to the deficiency of the atoms in the crystal lattice.

The electrical properties exhibited differences in the activation energy for the modified samples. Leaching conducted in the acid solvent induced decrease in the E_a value. Low activation energy could be related to higher quantity of the electric charge carriers and in turn of the resistivity decrease. The subsequent annealing procedure, conducted in the ambient air, led to increased E_a value comparable to the E_a estimated for the sample leached in the redistilled water.

The Brillouin light scattering data occurred for the transverse acoustic (TA) mode *vs.* Brillouin shift exhibited a phase transition of the pure and protonized lithium niobate samples (Figure 34). The value of the T_C was equal to 1120 °C and was lower than literature (T_C≈1140 °C) value of T_C that corresponded to deficiency of the lithium ions in the crystal. The proton exchange reaction did not have influence on the T_C value. It is worth to note, that Brillouin scattering is the volumetric measurement, which detectes an anomaly in protonized samples at the temperature T≈1050 °C. The volume of protonized surface layer, related to the depths of 380 nm, was sufficient enough to produce the significant response in longitudinal acoustic (LA) mode *vs.* Brillouin shift.

Further elaboration of the Brillouin scattering data is dependent on the promised cooperation with laboratory from Hallym University.

To estimate effects of thermal treatment of the lithium niobate, surface sensitive studies were conducted.

The *as-received* $LiNbO_3$ was analyzed by the XPS test at the room temperature and in high temperature range. Samples were measured in order to determine the chemical composition of the crystal. The significant deficiency of the lithium ions was detected at the RT in the crystal with epi-polished surface, the concentration was given by the [Li]/[Nb]=0.04 ratio. The ratio obtained for the cleaved surface of the crystal was equal to [Li]/[Nb]=0.67. Differences between the resulted [Li]/[Nb] ratio, in terms of literature data [Li]/[Nb]=0.94, may indicate the existence of easy diffusion paths [11]. Identification of the type of the diffusion kinetic is an open subject for the future measurement. It is worth to verify the model of diffusion in a dislocation network [17] which was observed for the model double oxide material which is $SrTiO_3$.

On one hand, we discovered that the marked deficiency of the Li ions in the surface could have been related to the leaching reaction when samples were polished, on the other hand, the Li deficiency diminished after the samples were treated in high temperature in UHV conditions. In this case, when samples were exposed to low pressure environment, migration of the Li and O ions from bulk toward the outermost surface layers was induced. Moreover,

part of these ions evaporated to the gaseous phase. The O, Li_2O, and O_2 compounds were detected over the crystal surface and identified with the use of the effusion test. The concentration of the other compounds, *e.g.*, Li, LiO, and NbO, was one or two orders of magnitude lower.

It was noticed that such a diffusion proceeded in non-equilibrium conditions and the goal of research was to determine the surface layer features, not the study of equilibrium processes themselves. Moreover, possible volatile products, responsible for mass loss in the TGA procedure, could have been different from those identified by effusion test.

In case of measurements conducted in the high temperature range from the 300 to 900 °C, the results of the XPS tests indicated that the structure of the surface layer transformed. It occurred that carbon and oxygen contamination disappeared, only one doublet related to the Nb^{5+} placed in the $LiNbO_3$ crystal lattice remained. Moreover, the Li state emerged and was visible in the spectrum obtained for the crystal surface. Herein the following explanation is proposed. At high enough temperature range, the migration of the Li ions towards the outermost surface layer is stimulated. Part of the Li ions can fill the V_{Li} vacancies. In consequence, the number of clusters Nb_{Li}–V_{Li} decreases. Moreover, part of the lithium ions evaporates from the samples, in the form of the LiO and Li_2O (compare effusion results, Figures 44 and 45). We deduced that the samples, held at high temperature during the XPS measurement, had a surface layer, which contained much lower amount of the clustered defects [15]. Such a mechanism is consistent with the TOF-SIMS test results, obtained also in a high temperature range (see Figure 46). It should be also noted that in case of low temperature range, the niobium states in the NbO (Figure 38) was correlated to the Nb line which occurred in vicinity of the VB (Figure 40).

The comparison of thermogravimetry and effusion tests enabled to determine the microscopic mechanism related to the reduction conditions, which were applied for the $LiNbO_3$ samples. The $LiNbO_3$ samples studied herein became non–transparent (see Figure 21) after the reducing procedure, which was consisted with the increased amount of defects. In case of double oxides, it usually corresponded to oxygen deficiency occurrence. One can conclude that the mass loss, determined by thermogravimetry cannot be assigned to the evaporation of the $LiNbO_3$ units or to the Li–Nb–O crystallographic planes from the surface. On the contrary, the dominating release of oxygen and lithium ions occurred under reducing conditions.

We would like to point out that the results of the other experiment [20], which was carried out on the Ti–doped $LiNbO_3$ in Ar atmosphere, were also discussed in the frame of the

diffusion model. Ranganath and Wang studied the possibility of suppression of the lithium out–diffusion with respect to the content of the Ti doping. They deduced that the partial pressure of the $p_{(Li2O)}=10^{-8}$ bar at $T\approx1000$ °C was related to the occurrence of the lithium out–diffusion. It is worth noting that these values were comparable to the results obtained from the effusion test in our experiment.

The simulation of evaporation was carried out by Tsirlin [81] for the lithium niobate crystals exposed to argon gas at high temperature in the 1000–1600 K range. The highest partial pressure occurred for Li ions and Li_2O molecules. It was proposed that such results corresponded to migration of the Li ions from the bulk towards the surface, followed by evaporation.

The effect of the lithium deficiency corresponded with the non-homogeneous distribution of the Li and Nb elements (see Figs 38, 39, 46, and 50), determined with the use of the XPS and TOF-SIMS tests. Hence, Li ions segregation appeared in the surface layer due to diffusion process from inner layers of the crystal lattice towards the surface.

In a brief summary, I would like to point that:

1. The setup for protonization reaction was completed and patented.
2. Conditions of the $H_xLi_{1-x}NbO_3$ formation were determined and the Li^+/H^+ ion substitution was confirmed with using SIMS analysis from the depth profiles.
3. The rhombohedral structure of the pure $LiNbO_3$ and monoclinic structure of the $H_xLi_{1-x}NbO_3$ samples were determined by the XRD measurement.
4. Migration of the Li ions from the crystal to the solvent was detected by using the ICP-OES technique. Release of niobium ions was blocked by the H^+ ions substituted to the Li sublattice when the reaction was conducted in the acid solvent.
5. Electrical features obtained by protonization were partially reversed after annealing process in ambient air.
6. The deficiency of the lithium ions in the surface layer originated from lithium niobate crystal samples preparation conducted in aqueous solutions. This explanation is deduced from the leaching procedure.
7. Variation in the [Li]/[Nb] ratio values may indicate the existence of more complex forms than point defects, *e.g.*, the occurrence of easy diffusion paths.
8. The loss of mass in reduction process of the $LiNbO_3$ is related mainly to evaporation of lithium and oxygen ions.
9. The kinetics of mass losses depends on ratio of surface layer volume to bulk volume.

10. The non-homogeneity in the distribution of the Li and Nb ions, and granular structure of surface morphology were detected for the reduced lithium niobate crystals.
11. The outward diffusion of lithium, from bulk reservoir towards the surface, was saturated after 1–2 hours at 900–1000 °C.
12. The improvement of chemical composition of the surface layer could be achieved by thermal treatment conducted in a high temperature range, which induced the outward diffusion of the Li ions.

Appendix

List of Publications

1. J. Piecha, K. Szot, M. Pilch, I. Gruszka, and A. Molak,
   „Influence of proton exchange on $LiNbO_3$ crystals structure”,
   Ferroelectrics 466 (2014) 1–7.

2. J. Piecha, A. Molak, U. Breuer, M. Balski, and K. Szot
   „Features of surface layer of $LiNbO_3$ as-received single crystals: studied *in situ* on treatment samples modified by elevated temperature”,
   Solid State Ionics. 290 (2016) 31-39.

3. J. Piecha, M. Dabioch, U. Breuer, and A. Leonarska
   „Structural and electrical features induced by the leaching procedures on the $LiNbO_3$ crystalline powder samples”
   Phase Transitions. 2016 accepted, DOI: 10.1080/01411594.2016.1206541

Patent

Patent Number: PL406671-A1, Patent Assignee: UNIV SLASKI,
authors: GRUSZKA I; MOLAK A; PIECHA J
“*Apparatus for carrying out protonated crystals in solutions of inorganic acids, has flask connected to thermometer and tube through second tap, which includes radiator, and adapter connected with radiator and receiver* “.

List of oral presentation

1. E-MRS 2014 Fall Meeting (European Materials Research Society), Warszawa, Poland 15-19.09.2014r.
   "Redox reaction in surface layer of $LiNbO_3$ monocrystals" (20 min).
2. Wpływ Młodych Naukowców na Osiągnięcia Polskiej Nauki VIII Edycja, Poznań, Poland, 28.03.2015r.
   „Wpływ reakcji redox na warstwę powierzchniową niobianu litu" (15 min).
3. Wpływ Młodych Naukowców na Osiągnięcia Polskiej Nauki VIII Edycja, Gdańsk, Poland, 11.04.2015r.
   „Wymiana protonowa w monokrystalicznych ferroelektrykach" (15 min).
4. Ogólnokrajowa Konferencja Młodzi Naukowcy w Polsce – Badania i Rozwój, Poznań, Poland, 8.06.2015r.
   „Zmiany stechiometrii warstwy powierzchniowej niobianu litu wywołane reakcjami redukcji" (15 min).
5. Ogólnokrajowa Konferencja Młodzi Naukowcy w Polsce – Badania i Rozwój, Poznań, Poland, 10.06.2015r.
   „Wpływ warunków redukujących na własności elektryczne warstwy powierzchniowej niobianu litu" (15 min).
6. Presentation at Hallym University in South Korea, 05.11.2015r.
   "Surface layer features of as-received $LiNbO_3$ crystals modified by elevated temperature treatment" (50 min).
7. Cracow Symposium on Physics and Chemistry of Materials, CSPCM2016, Kraków, Poland, 6.05.2016r.
   „Study of $LiNbO_3$ lithium deficiency" (15 min).

List of poster presentation

1. International Meeting on Ferroelectricity (IMF – 13), Kraków, 2-6.09.2013.
   "Influence of proton exchange on $LiNbO_3$ crystals structure",
2. Pomiędzy Naukami – zjazd fizyków i chemików, Chorzów, 27.09.2013.
   „Electronic structure of $LiNbO_3$ and $LiTaO_3$ reference and acid etching crystals"
3. Pomiędzy Naukami – zjazd fizyków i chemików, Chorzów, 26.09.2014.
   „Zmiany właściwości monokryształów niobianu litu indukowane reakcjami redox"
4. Pomiędzy Naukami – zjazd fizyków i chemików, Chorzów, 18.09.2015.
   „Stabilność stechiometrii w warstwie powierzchniowej niobianu litu"
5. XXII Polish-Czech Seminar: Structural and Ferroelectric Phase Transitions, Hucisko, Poland 16-20.06.2016.
   „Structural and electrical features induced by the leaching procedures on the $LiNbO_3$ crystalline powder samples"

List of Figures

List of Tables

References

[1] M. E. Lines and A. M. Glass, *Principles and applications of ferroelectrics and related materials*, Oxford Science Publications, Clarendon Press, Oxford, 1977.

[2] J. F. Nye, *Physical Properties of Crystals Their Representation by Tensors and Matrices*, Oxford Science Publications, Clarendon Press, Oxford, 1985.

[3] R. Blinc, *Advance Ferroelectricity*, Oxford University Press, 2011.

[4] A. Chełkowski, *Fizyka Dielektryków*, Warszawa 1993.

[5] C. Noguera, *Physics and Chemistry at Oxide Surfaces*, Cambridge University Press, 1996.

[6] V. Ya. Shur, *Domain Nanotechnology in Ferroelectric Single Crystals: Lithium Niobate and Lithium Tantalate Family*, Ferroelectrics 443 (2013) 71–82.

[7] M. A. Dolbilov, V. Ya. Shur, E. I. Shishkin, M. F. Sarmanova, E. V. Nikolaeva, S. Tascu, P. Baldi, and M. P. de Micheli, *Influence of surface layers modified by proton exchange on domain kinetics of lithium niobate*, Ferroelectrics 374 (2008) 14–19.

[8] K. Szot, W. Speier, J. Herion, and C. Freiburg, *Restructuring of the surface region in $SrTiO_3$*, Appl. Phys. A 64 (1997) 55–59.

[9] R. Waser, R. Dittmann, G. Staikov, and K. Szot, *Redox-based resistive switching memories–nanoionic mechanisms, prospects, and challenges*, Adv. Mater. 21 (2009) 2632–2663.

[10] P. J. Jorgensen and R.W. Bartlett, High temperature transport processes in lithium niobate, J. Phys. Chem. Solids. 30 (1969) 2639–2648.

[11] K. Szot, G. Bihlmayer, and W. Speier (Eds.), *Nature of the Resistive Switching Phenomena in TiO_2 and $SrTiO_3$: Origin of the Reversible Insulator – Metal Transition*, Solid. St. Phys. 65, 2014, pp. 353–559.

[12] K. G. Karapetyan, A. A. Kteyan, and R. A. Vardanyan, *Thermal reduction effect on Curie temperature of $LiNbO_3$ ferroelectrics*, Solid. St. Commun. 140 (2006) 474–476.

[13] A. Nowak, J. Persson, B. Schmelzer, J. Szade, and K. Szot, *Low temperature reduction in Ta–O and Nb–O thin films*, J. Phys. D: Appl. Phys. 47 (2014) 135301.

[14] T. Volk, M. Wöhlecke, *Lithium Niobate Defects, Photorefraction and Ferroelectric Switching, Springer Series in Materials Science*, Springer-Verlag Berlin Heidelberg, 2008.

[15] Y. Li, W. G. Schmidt, and S. Sanna, *Defect complexes in congruent $LiNbO_3$ and their optical signatures*, Phys. Rev. B 91 (2015) 174106–9.

[16] H. Donnerberg, S. M. Tomlinson, C. R. A. Catlow, and O. F. Schirmer, *Computer-simulation studies of intrinsic defects in $LiNbO_3$ crystals*, Phys. Rev. B 40 (1989) 11909–11916.

[17] K. Szot, W. Speier, R. Carius, U. Zastrow, and W. Beyer, *Localized metallic conductivity and self-healing during thermal reduction of $SrTiO_3$,* Phys. Rev. Lett. 88 (2002) 075508–4.

[18] C. Rodenbücher, *Thesis*, FZ, Juelich, (2014).

[19] J. Shi, H. Fritze, G. Borchardt, and K- D. Becker, *Defect chemistry, redox kinetics, and chemical diffusion of lithium deficient lithium niobate,* Chem. Phys. 13 (2011) 6925–6930.

[20] T. R. Ranganath and S. Wang, *Suppression of Li_2O out-diffusion from Ti-diffused $LiNbO_3$ optical waveguides*, Appl. Phys. Lett. 30 (1977) 376–379.

[21] L. F. Johnson and A. A. Ballman, *Coherent Emission from Rare Earth Ions in Electro-optic Crystals,* J. Appl. Phys., 40 (1969) 297-302.

[22] G. Dhanaraj, K. Byrappa, V. Prasad, and M. Dudley (Eds.): *Springer Handbook of Crystal Growth. Springer*, Springer-Verlag Berlin Heidelberg 2010.

[23] S. C. Abrahams and P. Marsh, *Defect structure dependence on composition in lithium niobate,* Acta Crystallogr., Sect. B: Struct. Sci. 42 (1986) 61–68.

[24] R. S. Weis and T. K. Gaylord, *Lithium niobate: summary of physical properties and crystal structure*, Appl. Phys. A. 37 (1985) 191–203.

[25] V. Hinkov, M. Barth, and K. Dransfeld, *Acoustic Properties of Proton Exchanged $LiNbO_3$ Investigated by Brillouin Scattering*, Appl. Phys. A. 38 (1985) 269–273.

[26] K. Gallo, C. B. E. Gawith, I. T. Wellington, S. Mailis, R. W. Eason, P. G. R. Smith, D. J. Richardson, and S. M. Kostritskii, *Ultraviolet writing of channel waveguides in proton-exchanged $LiNbO_3$*, J. Appl. Phys. 101 (2007) 014110-1–3.

[27] K. Gallo, A. Pasquazi, S. Stivala, and G. Assanto, *Parametric Solitons in Two-Dimensional Lattices of Purely Nonlinear Origin,* Phys Rev Lett. 100 (2008) 053901–1–4.

[28] I. E. Barry, G. W. Ross, P. G. R. Smith, and R. W. Eason, *Fabrication of Ridge Waveguides in Lithium Niobate by Differential Etching Following Spatially Selective Domain Inversion*, Univ. Southampton ORC Paper. 1717 (1999) 1–5.

[29] M. Manzo, *Influence of selective proton exchange on periodically poled lithium niobate: Properties of Lithium Niobate*. Stockholm: Sweden. 2010: 19–35.

[30] C. Canali, A. Carnera, G. Della Mea, P. Mazzoldi , S. M. Al Shukri, A. C. G. Nutt, and R. M. De La Rue, *Structural characterization of proton exchanged $LiNbO_3$ optical waveguides*, J. Appl. Phys. 59 (1986) 2643–2649.

[31] Z. Ren, P. J. Heard, K. R. Hallam, A. Wotherspoon, Q Jiang, R. Varrazza, and S. Yu, *Fabrication and characterizations of proton-exchanged $LiNbO_3$ waveguides fabricated by inductively coupled plasma technique*, Appl. Phys. Lett. 88 (2006) 142905–1–3.

[32] G. R. Paz-Pujalt, D. D. Tuschel, G. Braunstein, T. Blanton, S. Tong Lee, and L. M. Salter, *Characterization of proton exchange lithium niobate waveguides*, J. Appl. Phys. 76 (1994) 3981–3987.

[33] S. M. Neumayer, M. Manzo, A. L. Kholkin, K. Gallo, and B J. Rodriguez, *Interface modulated currents in periodically proton exchanged Mg doped lithium niobate*, J Appl. Phys. 119 (2016) 114103–1–7.

[34] J. L. Jackel, C. E. Rice, and J. J. Veselka, *Proton exchange for high index waveguides in $LiNbO_3$*, Appl. Phys. Lett. 41 (1982) 607–608.

[35] T. Ohsaka, M. Abe, Y. Kanzaki, T. Kotani, and S. Awano, *Synthetic inorganic ion Exchange materials XLIV: Synthesis and ion exchange properties of cubic niobic acid ($HNbO_3$)*, Materials Research Bulletin. 34 (1999) 1441–1450.

[36] T. Ohsaka, Y. Kanzaki, and M. Abe, *Irreversible Li^+/H^+ ion-exchange reaction between cubic $HNbO_3$ and rhombohedral $LiNbO_3$ and NMR study of $Li_xH_{1-x}NbO_3$*, Materials Research Bulletin. 36 (2001) 2141–2154.

[37] S. Kar, S. Verma, M. W. Shaikh, and K. S. Bartwal, *Effect of proton exchange and annealing on diffraction efficiency of Fe: $LiNbO_3$ crystals*, Physica B. 404 (2009) 3507–3509.

[38] M. De Micheli, J. Botineau, S. Neveu, P. Sibillot, and D. B. Ostrowsky, *Independent control of index and profiles in proton-exchanged lithium niobate guides*, Op. Lett, 8 (1983) 114–115.

[39] K. Gallo, *Dispositivi quadratici con quasi-accordo di fase in guide d'onda a scambio protonico in niobato di litio*, Dottorato di Ricerca in Ingegneria Elettronica, Informatica e delle Telecomunicazioni XIII ciclo, Universita' Degli Studi di Palermo, Facoltà di Ingegneria, 12 feb 2001.

[40] K. Tabata, T. Choso, and Y. Nagasawa, *The topmost structure of annealed single crystal of $LiNbO_3$*, Surf. Sci. 408 (1998) 137–145.

[41] O. F. Schirmer, O. Thiemann, and M. Wohlecke, *Defects in $LiNbO_3$—I. experimental aspects*, J. Phys. Chem. Solids 52 (1991) 185–200.

[42] H. Hatano, Y. Liu, and K. Kitamura, *Photorefractive Materials and Their Applications*, in Springer Series in Optical Sciences, *Growth and Photorefractive Properties of Stoichiometric $LiNbO_3$ and $LiTaO_3$*, 144 (2007) 127–164.

[43] J. Maier, *Physical Chemistry of Ionic Materials: Ion and Electrons in Solids*, John Wiley & Sons, England, 2004.

[44] J. Maier, J. Jamnik, and M. Leonhardt, *Kinetics of oxygen stoichiometry changes*, Solid State Ionics, 129 (2000) 25–32.

[45] J. Piecha, A. Molak, U. Breuer, M. Balski, and K. Szot, *Features of surface layer of $LiNbO_3$ as-received single crystals: Studied in situ on treatment samples modified by elevated temperature*, Solid State Ionics 290 (2016) 31–39.

[46] D. M. Smyth, *The role of impurities in insultating transition metal oxides*, Prog. Solid State Chem. 15 (1984) 145–171.

[47] S. C. Abrahams and P. Marsh, *Defect structure dependence on composition in lithium niobate*, Acta Crystallogr. Sect. B 42 (1986) 61–68.

[48] N. Iyi, K. Kitamura, F. Izumi, J. K. Yamamoto, T. Hayashi, H. Asano, and S. Kimura, *Comparative study of defect structures in lithium niobate with different compositions*, J. Solid State Chem. 101 (1992) 340–352.

[49] N. Kumada, N. Ozawa, F. Muto, and N. Kinomura, *$LiNbO_3$ with ilmenite-type structure prepared via ion-exchange reaction*, J. Solid State Chem. 57 (1985) 267–268.

[50] J. Maier, *Complex oxides: high temperature defect chemistry vs. low temperature defect chemistry*, Phys. Chem. Chem. Phys., 5 (2003) 2164–2173.

[51] D. M. Smyth, *Defects and transport in $LiNbO_3$*, Ferroelectrics 50 (1983) 93-102.

[52] L. G. Harrison, *Influence of dislocations on diffusion kinetics in solids with particular reference to alkali halides*, Faraday Soc., 57 (1961) 1191-1199.

[53] J. Piecha, K. Szot, M. Pilch, I. Gruszka, and A. Molak, *Influence of Proton Exchange on $LiNbO_3$ Crystals Structure*, Ferroelectrics 466 (2014) 1–7.

[54] J. Piecha, M. Dabioch, U. Breuer, and A. Leonarska, *Structural and electrical features induced by the leaching procedures on the $LiNbO_3$ crystalline powder samples*, Phase Transit., 2016 DOI: 10.1080/01411594.2016.1206541.

[55] P. van der Heide, *Secondary Ion Mass Spectrometry An introduction to Principles and Practices*, Wiley, 2014.

[56] http://www.fz-juelich.de/zea/zea-3/EN/Leistungen/AnalytischeVerfahren/Lokalisierung/SIMS.html.

[57] A. Kachel, *XP Program Guide*,1995.

[58] J. Rodriguez–Carvajal, *Introduction to the Program Fullprof* (2006).

[59] R. Saravanan, T. K. Thirumalaisamy, and T. Kajitani, *Local structure determination of the nonlinear optical material $LiNbO_3$ using XRD*, Phys. Status Solidi A 208 (2011) 2643–2650.

[60] J. H. Kim, J. Y. Choi, M. S. Jeong, J. H. Ko, M Ahart, Y. H. Ko, and K. J. Kim, *Development of a high-pressure brillouin spectrometer and its application to an ethylene-vinyl acetate copolymer*, J. Korean Phys Soc. 62 (2012) 1419–1423.

[61] B. W. Lee, J. Ryeom, Y. H. Ko, K. J. Kim, and J.-H. Ko, *Acoustic anisotropy of oriented polyethylene terephthalate films studied through Brillouin light scattering*, J. Inf. Disp. 15 (2014) 201–205.

[62] F. Kremer and A. Schonhals, *Broadband dielectric spectroscopy*, Berlin: Springer Verlag; 2002 [chapter 3].

[63] P. Heitjans, M. Masoud, A. Feldhoff, and M. Wilkening, *NMR and impedance studies of nanocrystalline and amorphous ion conductors: lithium niobate as a model system*, Royal Society of Chemistry 134 (2007) 67–82.

[64] D. L. Staebler and J. J. Amodeia, *Thermally fixed holograms in $LiNbO_3$*, Ferroelectrics 3 (1972) 107–113.

[65] N. S. Hari, P. Padmini, and T. R. N. Kutty, *Complex impedance analyses of n-$BaTiO_3$ ceramics showing positive temperature coefficient of resistance*, J Mater Sci–Mater El. 8 (1977) 15–22.

[66] M. Pilch and A. Molak, *Resistivity switching induced in ferroelectric phase of $PbTiO_3$ studied by XPS and electric conductivity tests*, J. Alloy Compd. 586 (2014) 488–498.

[67] D. C. Sinclair and A. R, West, *Impedance and modulus spectroscopy of semiconducting $BaTiO_3$ showing positive temperature coefficient of resistance*, J. Appl. Phys. 66 (1989) 3850–3856.

[68] Y. L. Chen and S. F. Yang, *PTCR effect in donor doped barium titanate: review of compositions, microstructures, processing and properties*, Adv. Appl. Ceram. 110 (2011) 257–269.

[69] A. de Bernabé, C. Prieto, and A. de Andrés, *Effect of stoichiometry on the dynamic mechanical properties of $LiNbO_3$*, J. Appl. Phys. 79 (1996) 143–148.

[70] M. Aufray, S. Menuel, Y. Fort, J. Eschbach, D. Rouxel, and B. Vincent, *New synthesis of nanosized niobium oxides and lithium niobate particles and their characterization by XPS analysis*, J. Nanosci. Nanotech. 9 (2009) 4780–4785.

[71] P. Steiner and H. Hochst, *X-ray excited photoelectron spectra of $LiNbO_3$: A quantitative analysis*, Z. Physik B, 35 (1979) 51–59.

[72] M.L. Shek, J. Hrbek, T. K. Sham, and G. Q. Xu, *A soft X-ray study of the interaction of oxygen with Li*, Surf. Sci. 234 (1990) 324–334.

[73] N. Kaufherr, D. J. Eichorst, and A. Payne, *X-ray photoelectron spectroscopy studies of alkoxide-derived lithium niobate*, J. Vac. Sci. Technol. A 14 (1996) 299–305.

[74] J. F. Moulder, W. F. Stickle, P. E. Sobol, and K. D. Bomben, *Handbook of X-ray Photoelectron Spectroscopy*, Physical Electronics, Inc. United States of America, 1995.

[75] C. D. Wagner, *Sensitivity of detection of the elements by photoelectron spectrometry*, Analytical Chemistry 44 (1972) 1050–1053.

[76] S. Mamoun, A. E. Merad, and L. Guilbert, *Energy band gap and optical properties of lithium niobate from ab initio calculations*, Comp. Mater. Sci. 79 (2013) 125–131.

[77] R. Courths, P. Steiner, H. Hoechst, and S. Hüfner, *Photoelectron-spectroscopy investigation and electronic properties of $LiNbO_3$ crystal surfaces*, Appl. Phys. 21 (1980) 345–352.

[78] V. E. Henrich, *The surfaces of metal oxides*, Rep. Prog. Phys. 48 (1985) 1481–1541.

[79] A. Molak, K. Szot, A. Kania, J. Friedrich, and H. J. Penkalla, *Insulator–metal transition in Mn-doped $NaNbO_3$ induced by chemical and thermal treatment*, Phase Transit. 81 (2008) 977–986.

[80] J. R. Carruthers, I. P. Kaminov, and L. W. Stulz, *Diffusion kinetics and optical waveguiding properties of outdiffused layers in lithium niobate and lithium tantalite,* Appl. Optics 13 (1974) 2333–2342.

[81] M. Tsirlin, *Influence of gas phase composition on the defects formation in lithium niobate*, J. Mater. Sci. 39 (2004) 3187–3189.